Topics in Catalysis
https://doi.org/10.1007/s11244-026-02322-0

REVIEW PAPER

Photocatalytic NO_x Oxidation and Storage: An Alternative Technology for Airborne NO_x Abatement Beyond the Point of Production

Rukiye Babacan Tosun[1] · Ali Dortbudak[1] · Emrah Ozensoy[1,2]

Accepted: 9 June 2026

Abstract
Airborne nitrogen oxides (NO_x) are among the most persistent urban pollutants, contributing to ozone formation, acid rain, and respiratory health issues. Beyond emission control at the source, photocatalytic NO_x oxidation and storage (PHONOS) has emerged as a promising strategy for sustainable environmental remediation. This review systematically discusses the fundamental mechanisms, material developments, and practical aspects of photocatalytic NO_x abatement. We first summarize the reaction pathways governing NO and NO_2 oxidation on TiO_2 and related semiconductors, emphasizing the roles of photogenerated holes, hydroxyl radicals, and surface-bound intermediates in determining selectivity toward nitrate. Next, we highlight advances in material design, including single-atom catalysts, doped TiO_2, g-C_3N_4 heterostructures, and oxygenate-modified surfaces that enhance visible-light activity and nitrate storage stability. The influence of environmental factors-such as humidity, reactant gas flow rate, and irradiation wavelength are also discussed. Existing scientific literature suggests that as a novel environmental airborne pollution abatement technology, PHONOS has the potential to evolve from a laboratory concept into a viable, sunlight-driven approach for actively improving urban air quality even far away from the point where pollution is generated.

Keywords Photocatalytic NO_x oxidation-storage · $DeNO_x$ · TiO_2 · g-C_3N_4 · UV/Vis-driven systems

1 Introduction

Nitrogen oxides (NO_x), particularly nitric oxide (NO) and nitrogen dioxide (NO_2), are among the most critical atmospheric pollutants, primarily emitted by fossil fuel combustion in the transportation, power generation and manufacturing industry, while natural sources such as lightning and microbial activity also contribute to NO_x emissions [1]. NO_x species significantly degrade air quality in urban environments due to their formation of photochemical smog, ground-level ozone (O_3), and secondary particulate matter ($PM_{2.5}$) [2, 3]. Prolonged exposure to NO_2 is intricately linked to asthma, other respiratory conditions, and cardiovascular diseases [4]. The World Health Organization (WHO) and the European Union (EU) have established annual air quality guideline (AQG) levels 10 μg/m^3 and 40 μg/m^3, respectively, for NO_2; however urban concentrations in many cities still exceed these thresholds [5, 6].

From 1970 to 2022, global NO_x emissions increased from an average of 324 gigagrams (Gg) to approximately 500 Gg (Fig. 1) [7]. Although there was a slight decrease in emissions in 2020 due to the Covid-19 pandemic, these values continued to rise in recent years. Considering NO_x emission levels in 2022, countries such as the USA, China, Russia, and Brazil are among the leading contributors. Furthermore, contribution from middle-income and developing countries to global NO_x emission levels remains substantial [7–9].

From 2013 to 2020, New Delhi's average annual NO_2 levels ranged from 61 to 74 =μg/m^3. In Japan, average annual NO_2 level was measured to be 26 μg/m^3. In 2023, some of the highest NO_2 values in Europe were measured to be 53 μg/m^3 at the Na07 Ente Ferrovie station (Italy), 69 μg/m^3 at Patision (Greece), 107 μg/m^3 at Ankara-Ulus (Turkey), 49 μg/m^3 at Katowice (Poland), and 44 μg/m^3 at the Lyon Périphérique station (France) [6]. Driven by

✉ Emrah Ozensoy
ozensoy@fen.bilkent.edu.tr

[1] Chemistry Department, Bilkent University, 06800 Ankara, Türkiye

[2] UNAM-National Nanotechnology Center, Bilkent University, 06800 Ankara, Türkiye

Published online: 24 July 2026

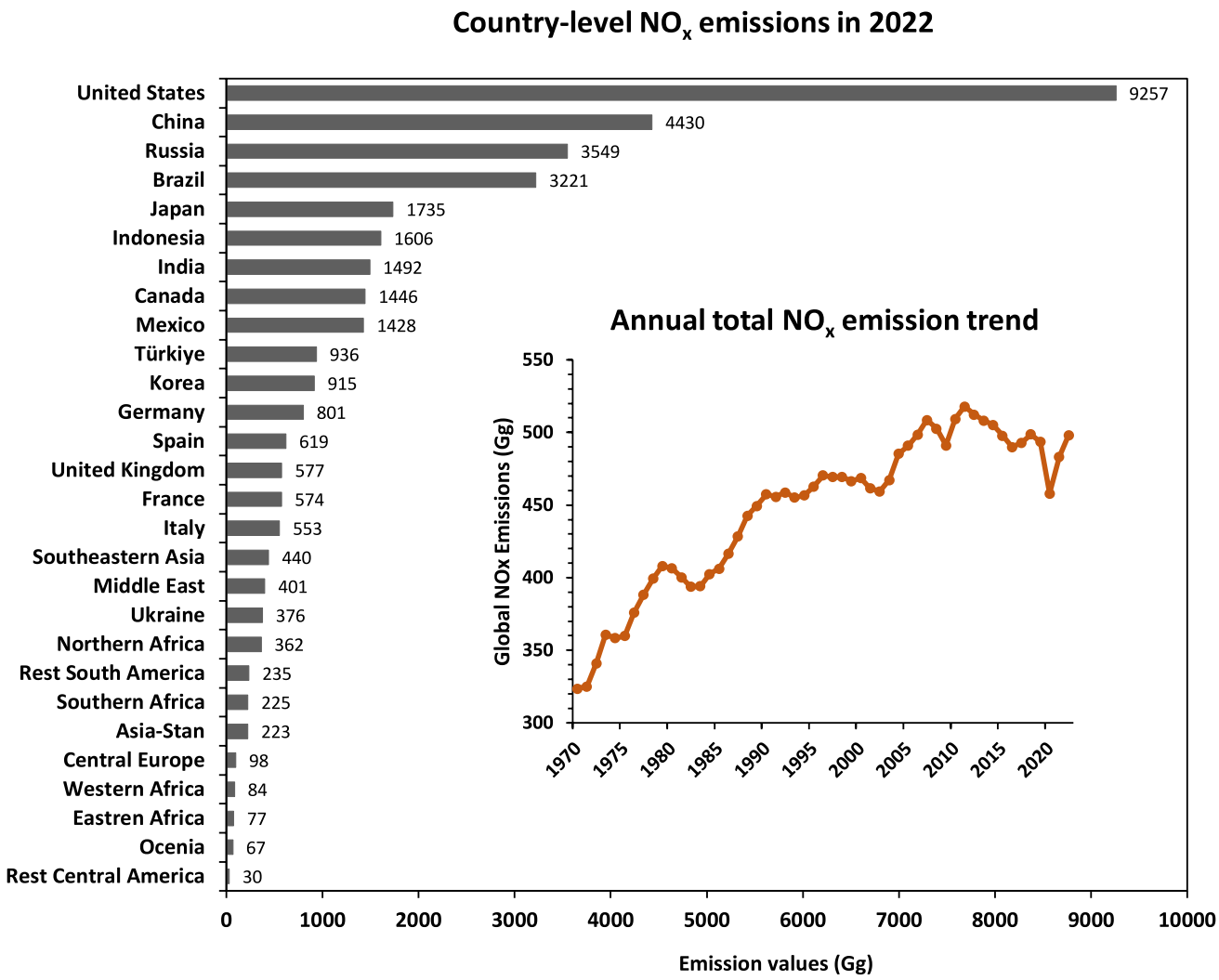

Fig. 1 NO_x emissions by country in 2022, with an inset showing the global trend in total NO_x emissions from 1970 to 2022 [7]

increasingly stringent environmental legislation, research into the elimination of NO_x species and the development of more efficient engines has accelerated [10].

Nitric oxide (NO), the primary component of NO_x emissions, does not readily decompose under ambient or exhaust conditions due to the high activation energy associated with its direct gas-phase decomposition ($2NO \rightarrow N_2 + O_2$), which is ca. 350 kJ/mol. Although thermodynamically feasible, this reaction is kinetically inhibited [11]. Consequently, extensive research efforts have been devoted to developing catalytic systems capable of lowering the kinetic barrier and promoting the selective conversion of NO_x to N_2 [12]. Conventional NO_x abatement ($DeNO_x$) technologies, including three-way catalytic converters (TWC), NO_x storage and reduction (NSR)/lean NO_x trap (LNT), selective catalytic reduction (SCR), and non-thermal plasma reactors, have been widely applied for stationary and mobile sources [13].

Despite their effectiveness under controlled operating conditions, these technologies remain largely confined to emission-control systems located at the source of NO_x generation. TWCs are fundamentally restricted to a narrow stoichiometric window and become ineffective under oxygen-rich conditions, while NSR catalysts are highly vulnerable to sulfur poisoning and require periodic rich operation that compromises durability and fuel efficiency [14–26]. Although SCR enables continuous NO_x reduction under lean exhaust, its reliance on an external reductant, complex control strategies, and limited low-temperature activity introduces additional operational and secondary emission challenges [27–35]. As a result, the applicability of these technologies to ambient-air purification is inherently limited.

Once emitted into the atmosphere, NO and NO_2 persist for hours or even days, undergoing complex photochemical transformations that contribute to ozone and nitrate aerosol

formation [36, 37]. Therefore, an urgent need exists for passive, low-energy, and widely deployable technologies capable of removing NO_x beyond the point of production, i.e., after their dispersion in the ambient air.

In this context, photocatalytic NO_x oxidation and storage (PHONOS) emerges as a promising green $DeNO_x$ technology for airborne NO_x abatement. During PHONOS, photocatalyst enables the oxidation of NO_x followed by its storage on the catalyst surface as solid-state nitrate species [38–40]. This process is driven by light irradiation, which can be readily supplied by ambient or solar radiation. Unlike conventional thermally driven $DeNO_x$ technologies that rely on continuous thermal energy input to maintain high operating temperatures, photocatalytic systems can operate passively under outdoor conditions. This feature makes them particularly attractive for real-world applications such as building facades, pavements, and indoor air-purification devices [41], where continuous PHONOS can be achieved under natural solar illumination. However, the overall efficiency of the process depends on factors such as light intensity, catalyst activity, and environmental conditions, which must be carefully considered for practical implementation.

The photocatalytic process resembles the natural self-cleaning capacity of the Earth's troposphere, where solar UV radiation initiates homogeneous photochemical reactions leading to the formation of highly reactive hydroxyl radicals (·OH), often referred to as the "detergent" of the atmosphere [42]. In the troposphere, OH radicals are primarily generated via ozone photolysis ($O_3 + h\nu \rightarrow O(^1D) + O_2$) followed by reaction with water vapor ($O(^1D) + H_2O \rightarrow 2{\cdot}OH$) [43]. Similarly, in heterogeneous photocatalysis, photoexcitation generates electron–hole pairs (e^-/h^+) [44]. The photogenerated holes (h^+) oxidize adsorbed H_2O or OH^- to produce hydroxyl radicals (·OH), while electrons (e^-) reduce O_2 to superoxide radicals ($O_2^-{\cdot}$). These reactive oxygen species drive the stepwise oxidation of NO to NO_2 and ultimately to surface-bound nitrate (NO_3^-) [41, 44]. Thus, the oxidative chemistry underlying PHONOS is conceptually similar to that operating in the troposphere, where reactive oxygen species govern NO_x conversion.

$$TiO_2 + h\nu \rightarrow TiO_2\left(h^+\right) + TiO_2\left(e^-\right) \quad (1)$$

$$h^+ + H_2O_{ads} \rightarrow {\cdot}OH_{ads} + H^+ \quad (2)$$

$$e^- + O_{2,ads} \rightarrow O_2^-{\cdot} \quad (3)$$

Since the pioneering work of Fujishima and Honda in 1972, who demonstrated the photoelectrochemical splitting of water on a TiO_2 electrode under UV irradiation, TiO_2-based photocatalysts have been extensively investigated [45]. In their seminal study, a TiO_2 photoanode coupled with a Pt cathode enabled the electrolysis of water into H_2 and O_2 at a significantly reduced bias voltage compared with conventional electrolysis, due to UV-induced photoexcitation. Upon UV irradiation, TiO_2 generates photogenerated electron–hole pairs, which subsequently react with O_2 and H_2O on the catalyst surface to form reactive oxygen species (Eq. *1–3*) [45–49]. This discovery laid the foundation for the widespread exploration of TiO_2 in photocatalytic applications, including environmental purification, self-cleaning surfaces, and antibacterial coatings [48]. Early work by Ibusuki and Takeuchi demonstrated that UV-illuminated TiO_2 (P25, ca. 80% anatase and 20% rutile) enables the removal of low-concentration NO/NO_2–N_2 mixture (1–2 ppm) from air over a wide range of relative humidities (0 to 72% RH at 310 K) [50]. TiO_2/activated carbon mixture (2:1, wt.%) suppresses NO_2 release by adsorbing intermediate NO_2 and prolonging its residence time for further oxidation, and Fe_2O_3 acts as a promoter, with surface nitrate accumulation being completely removed by simple water washing [50]. Negishi et al. demonstrated that TiO_2 thin films with distinctly different nano and micro scale surface morphologies, prepared via polymer-assisted sol–gel dip-coating, exhibit comparable NO removal efficiencies under UV irradiation [51]. Critically, the results indicate that controlling surface morphology alone is insufficient to significantly control NO_2 desorption behavior during photocatalytic NO oxidation [51]. These reports showed that one of the critical issues in NO_x photocatalysis is the formation and potential release of NO_2 during the reaction. While the overarching goal is the complete conversion of NO to stable surface-bound nitrate, incomplete oxidation or unfavorable reaction conditions may lead to secondary NO_2 emission, a pollutant significantly more toxic than NO, as evidenced by its nearly order-of-magnitude lower exposure limits (~1–3 ppm for NO_2 vs. ~25 ppm for NO) and pronounced acute respiratory effects [52]. Surface-triggered HONO (nitrous acid) release, particularly under humid conditions, further complicates the environmental profile of photocatalytic systems [53]. HONO is a key precursor to hydroxyl radicals (·OH) in the troposphere and contributes to early-morning photochemical smog formation [54]. These side pathways highlight the delicate interplay between surface chemistry, reaction intermediates, and environmental factors such as humidity, oxygen availability, and flow dynamics.

Beyond selectivity challenges, a major bottleneck in NO_x photocatalysis is nitrate storage and long-term stability. While nitrate formation is the desired outcome, excessive accumulation may lead to catalyst surface saturation, deactivation, and eventual release of stored NO_x species under fluctuating humidity or thermal conditions. This underscores a fundamental paradigm: NO_x photocatalysis involves not only oxidation but also storage and potential

release processes, all of which must be carefully controlled to develop robust and environmentally safe $DeNO_x$ technologies.

Due to its relatively weak adsorption on metal oxide surfaces, NO cannot be efficiently stored in its molecular form and must first be oxidized to NO_2, which can be more readily captured as surface nitrites or nitrates, as widely reported in NSR systems [55]. In conventional NSR catalysts, this later oxidation step is commonly thermally catalyzed at elevated temperatures (e.g., 200–400 °C) by noble metals under lean conditions, while the resulting nitrates predominantly accumulate on basic metal oxides such as BaO (in addition to the smaller extent of NO_x storage on the conventional γ-Al_2O_3 catalyst support material) [10]. Upon continuous NO_x adsorption, these storage sites become saturated, leading to a loss of NO_x storage capacity. Regeneration is therefore required. In NSR catalytic systems, regeneration is typically achieved at 200–450 °C by reducing stored nitrates to N_2 in the presence of precious metals (e.g., Pd, Pt), and using reducing agents such as CO, NH_3, hydrocarbons, or H_2 [40, 56].

However, efficient NO oxidation under ambient conditions remains challenging. This limitation can be overcome by integrating photocatalytic NO oxidation (e.g., via TiO_2) with NO_x storage components (e.g., alkali or alkaline-earth oxides), enabling effective NO_x removal under ambient conditions (Fig. 2) [40]. Deactivated $DeNO_x$ photocatalysts in outdoor settings can be regenerated at room temperature by removing surface/bulk nitrite and nitrate species via dissolution in water through the action of rain, restoring active sites and NO_x storage sites for further catalytic and adsorption processes [40, 57].

A critical yet underexplored dimension of NO_x photocatalysis is the role of experimental conditions in reported performance metrics. Numerous critical factors such as gas flow rate, residence time, humidity, NO/NO_2 feed composition, reactor design, irradiation geometry etc. all strongly influence observed photocatalytic selectivity and conversion. Literature exhibits significant variations or even absence of reporting of some of these essential parameters hindering accurate quantitative comparison of the published work. For instance, high flow rates may suppress NO_2 re-adsorption, inflating NO_2 emission, whereas low flow rates may boost conversion efficiency by favoring longer residence times. Similarly, humidity dramatically alters surface hydroxylation, NO_2 solubility, radical formation, and nitrate stability [40, 58]. Without standardized photocatalytic testing protocols, photocatalytic performance results from different reports cannot be precisely evaluated in a systematic manner.

This review focuses on the mechanistic aspects of PHONOS process, photocatalyst material development, and methodological considerations associated with photocatalytic performance measurements in PHONOS studies. We first discuss ultraviolet (UV)-active PHONOS systems, which serve as a mechanistic benchmark owing to their high oxidation capability and well-established reaction pathways. We then examine visible (VIS)-light-driven PHONOS systems, which offer improved practical relevance, but face challenges related to selectivity and charge-transfer

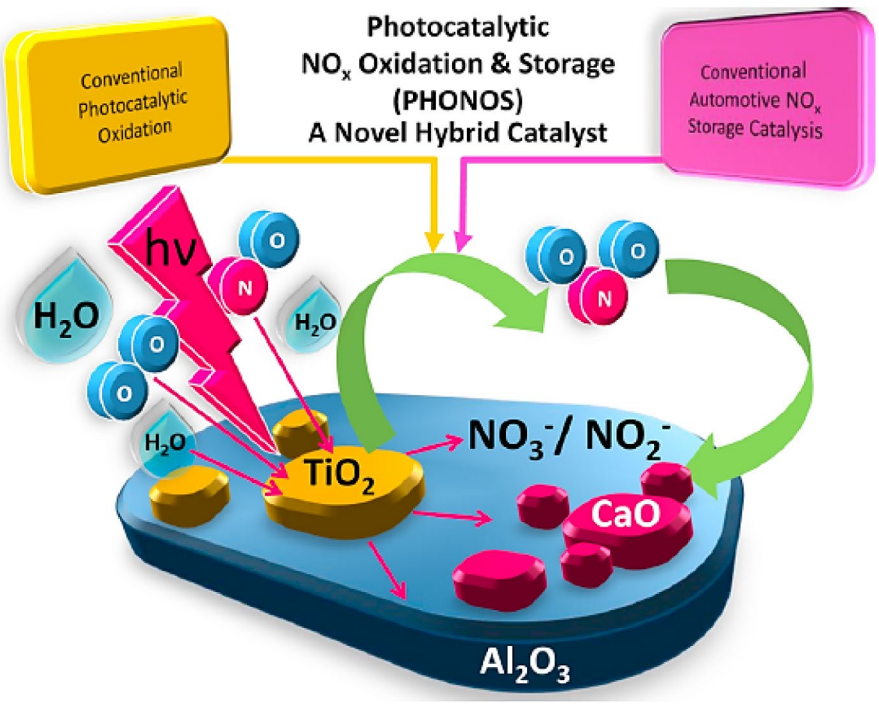

Fig. 2 Schematic view of hybrid Photocatalytic NO_x Oxidation and Storage (PHONOS) catalyst concept with enhanced NO_x(g) capture and improved $DeNO_x$ selectivity [40]. Copyright, 2020, Elsevier

limitations. Finally, broad-spectrum photocatalysts are evaluated with an emphasis on synergistic interactions between UV and VIS light. We believe that this critical review may inspire rational design of next-generation photocatalytic materials particularly for effective NO_x oxidation and storage under realistic environmental conditions.

2 Mechanistic Insights into Photocatalytic NO_x Oxidation and Storage

Under light irradiation, photocatalyst generates electron–hole (e^-/h^+) pairs, which migrate to the catalyst surface and initiate a series of redox reactions. Photogenerated holes react with adsorbed water molecules or surface hydroxyl groups to produce hydroxyl radicals (·OH), while photogenerated electrons reduce adsorbed oxygen to form superoxide species (O_2^-·); in addition, singlet oxygen ($^1O_2$) may also be generated under suitable conditions [59]. These reactive oxygen species (ROS), together with direct oxidation by photogenerated holes, play a key role in the oxidation of NO. The oxidation process proceeds primarily through the stepwise conversion of NO to NO_2, followed by further oxidation to nitrate species (NO_3^-), which are commonly retained on the photocatalyst surface. In TiO_2-based systems, irradiation with photons of energy equal to or greater than the band gap (for undoped anatase > 3.2 eV or λ < 380 nm) promotes electron excitation from the valence band to the conduction band, enabling these surface reactions (Fig. 3a) [60]. Overall, photocatalytic NO oxidation over TiO_2 has been demonstrated to be an efficient and cost-effective method for NO conversion, with NO_2 acting as a transient intermediate and NO_3^- as the dominant final product, as supported by previously reported reaction mechanisms and kinetic studies [61–65]. Based on these reactive species (i.e., ·OH and O_2^-·), the photocatalytic NO oxidation process can proceed via multiple pathways. Reactions (*4–16*) summarize representative steps reported in the literature [61–65]. In particular, reactions involving ·OH radicals (*4–6*) are primarily responsible for the stepwise oxidation of NO to NO_2 and HNO_3, while $\cdot O_2^-$ species contribute to the direct oxidation of adsorbed NO to nitrates (reaction *7*). In contrast, reactions containing photogenerated electrons (*10–16)* represent possible reduction and photodecomposition pathways of adsorbed NO_x species [66–68].

The photooxidation path:

$$NO + \cdot OH \rightarrow HNO_2 \quad (4)$$

$$HNO_2 + \cdot OH_{ads} \rightarrow NO_2 + H_2O \quad (5)$$

$$NO_2 + \cdot OH_{ads} \rightarrow HNO_3 \quad (6)$$

$$NO + \cdot O_{2,ads^-} \rightarrow NO_{3^-} \quad (7)$$

$$2NO + O_2 \rightarrow 2NO_2 \quad (8)$$

$$3NO_2 + 2OH^- \rightarrow 2NO_3^- + NO + H_2O \quad (9)$$

The photodecomposition path:

$$NO \rightarrow N_{ads} + O_{ads} \quad (10)$$

$$NO_{ads} + N_{ads} \rightarrow N_2O_{ads} \quad (11)$$

$$NO_{ads} + O_{ads} \rightarrow NO_{2,ads} \quad (12)$$

$$2O_{ads} \rightarrow O_{2,ads} \quad (13)$$

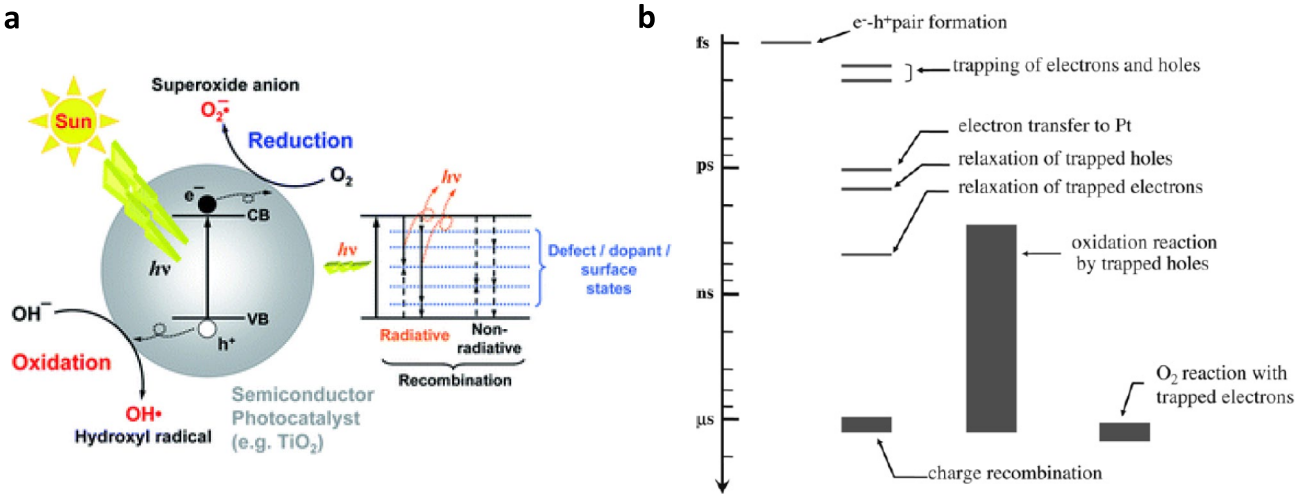

Fig. 3 **a** Schematic illustration of the photocatalytic mechanism of a typical semiconductor [60]. Copyright, 2014, RSC, **b** Temporal evolution of charge carrier processes in photocatalysis [44]. Copyright, 2008, Elsevier

$$2N_{ads} \rightarrow N_{2,ads} \quad (14)$$

$$2NO_{ads} \rightarrow O_{2,ads} + N_{2,ads} \quad (15)$$

$$2N_2O_{ads} \rightarrow O_{2,ads} + 2N_{2,ads} \quad (16)$$

While nitrate formation is widely considered the dominant pathway in TiO_2-mediated NO oxidation, cryotrapping-mass spectrometric analysis (CryoF/TQMS system) has revealed that N_2O can be the dominant product during UV-driven NO conversion over anatase TiO_2 at low relative humidity conditions [69]. Thus, photocatalytic generation of N_2O from NO in the presence of O_2 and H_2O has been reported to be negligible on titania photocatalyst [69].

Photocatalytic activity over TiO_2 is fundamentally governed by the generation, migration, and recombination of photogenerated charge carriers, while light absorption alone is insufficient to ensure efficient photocatalytic reactions [44, 48]. Early mechanistic studies revealed that electron–hole pairs generated upon UV irradiation undergo ultrafast recombination in the bulk on femtosecond (fs, 10^{-15} s) to picosecond (ps, 10^{-12} s) time scales, leaving only a small fraction of charge carriers available for surface reactions (Fig. 3b) [70, 71]. Subsequent investigations demonstrated that the overall photocatalytic efficiency is governed by the competition between charge carrier recombination and interfacial charge transfer, with bulk recombination occurring at rates significantly faster than surface redox processes [48, 72]. Therefore, photocatalytic reactions are dominated by long-lived charge carriers that successfully migrate to the surface and participate in interfacial chemistry. In TiO_2 non-radiative recombination pathways are predominant, with excitation energy being dissipated mainly as lattice vibrations rather than photon emission. Radiative recombination, commonly probed by photoluminescence spectroscopy, is therefore largely associated with defect- or trap-mediated states rather than intrinsic band-to-band transitions. Surface defects such as oxygen vacancies and Ti^{3+} centers exhibit a dual role: shallow trap states can temporarily capture charge carriers and prolong their lifetimes, whereas deep trap states act as recombination centers that promote non-radiative energy dissipation [70, 72]. Consequently, photocatalytic performance reflects a delicate balance between suppressing fast bulk recombination, optimizing surface defect chemistry, and facilitating efficient charge transfer to adsorbed reactants, which ultimately dictates the formation of reactive oxygen species and the overall rate of surface redox reactions, including NO oxidation.

3 UV-Driven Photocatalytic Systems for NO_x Oxidation and Storage

Despite the growing emphasis on visible-light-driven photocatalysis, ultraviolet (UV)-active systems continue to play a foundational role in the development and evaluation of photocatalytic NO_x abatement technologies. Historically, UV-responsive photocatalysts (most notably TiO_2) have served as mechanistic benchmarks, enabling detailed elucidation of reaction pathways, surface intermediates, and deactivation phenomena under well-controlled irradiation conditions [73, 74]. This benchmark status has been further reinforced by the development and widespread adoption of the ISO 22197-series standards regulating photocatalytic removal methodologies for different gas phase pollutants such as NO, acetaldehyde, toluene, and formaldehyde [75, 76].

The relevance of UV-active photocatalysts does not primarily stem from their suitability for real-world urban implementation, but rather from their ease of use in conventional experimental research studies. [44]. Wide bandgap metal oxide semiconductors ensure strong redox potentials, facilitating the generation of highly oxidative photogenerated holes and reactive oxygen species (ROS). These features make UV-driven systems ideal platforms for disentangling the fundamental steps of NO oxidation, nitrate formation, and surface accumulation.

However, the reliance on UV irradiation accounting for less than 5% of the solar spectrum-imposes severe constraints on scalability and sustainability [73]. As such, UV-active photocatalysts are regarded as reference and/or complementary systems rather than final solutions within the context of PHONOS and other solar-driven initiatives.

3.1 Pristine TiO_2

Pristine anatase TiO_2 is considered the most active TiO_2 phase for photocatalytic NO_x oxidation due to its indirect band gap which increasing electron–hole lifetime, its generally high specific surface area resulting from common synthesis protocols, and its abundance of surface hydroxyl groups [77]. Photon-induced holes formed in the anatase phase under UV irradiation interact with surface-adsorbed H_2O and OH^- species, facilitating the formation of ·OH radicals. These radicals then cause the sequential oxidation of adsorbed NO molecules to HONO, NO_2, and ultimately surface-bound nitrate species. However, despite its high NO conversion, anatase TiO_2 cannot completely prevent the release of the NO_2 intermediate into the gas phase under most conditions, leading to a selectivity problem [77, 78]. Furthermore, the accumulation of nitrate species on the surface over time can block the active sites, leading to a

decrease in performance in the steady-state regime after the transient high activity observed on anatase TiO_2 [49]. Mechanistic studies combining in-situ DRIFTS, TPD, and DFT have shown that NO_2 oxidation on anatase TiO_2 results in the formation of strongly bound surface nitrate species, including lattice-anchored NO_3^- and co-occurring adsorbed nitrate ions, which exhibit high thermal stability and can accumulate on the surface under UV irradiation, providing a mechanistic basis for their potential role in nitrate storage and secondary NO_x-related emissions [79].

Rutile-rich TiO_2 displays limited suitability for photocatalytic NO_x removal, as demonstrated by its low NO (~33%) and NO_x (~5%) conversions accompanied by very high NO_2 selectivity (~82%) after 10 h of under broadband (250–700 nm) UV–visible irradiation [80]. This behavior arises from the combined effects of direct band gap (3.0 eV) structure and low specific surface area (47.91 $m^2 g^{-1}$), resulting in a reduced surface hydroxyl density [62]. In addition, less efficient charge separation compared to anatase, rutile restricts the adsorption and subsequent oxidation of NO_2 intermediates, thereby favoring their release rather than their conversion into surface-bound nitrates [80]. Surface spectroscopic studies have shown that NO and NO_2 adsorption occurs on rutile TiO_2, but nitrate formation is more limited compared to anatase [81]. Therefore, rutile TiO_2 is rarely preferred in practical photocatalytic air purification applications due to its low NO_x conversion and poor long-term performance when used alone [62].

P25 (TiO_2) offers a more stable performance in photocatalytic NO_x removal compared to pure phases thanks to the synergistic combination of approximately 80% anatase and 20% rutile phases [64, 78]. Charge transfer occurring at the anatase–rutile interface enables photon-excited electrons to be directed to the rutile phase, thus suppressing electron–hole recombination [62]. While this synergy contributes to P25's increased NO conversion, a significant amount of NO_2 intermediate release is still observed, creating a potentially environmentally questionable benefit. Although P25-containing coatings have been shown to reduce NO and NO_2 concentrations in real-scale applications, limitations such as selectivity and surface nitrate deposition reveal that P25 alone is not an ideal solution [78].

Systematic pretreatment studies on P25 reveal that increasing calcination temperature from 70 °C to 600 °C results in a pronounced decrease in NO decomposition rates from approximately 1210 to 430 μmol h^{-1} g_{cat}^{-1}, highlighting the sensitivity of UV-driven activity to surface hydroxyl density. Under identical conditions, NO reduction in the presence of CO also declines with pretreatment severity, decreasing from 657 to 240 μmol h^{-1} g_{cat}^{-1}, indicating that both oxidative and reductive pathways are governed by surface-bound functionalities rather than bulk phase alone. Selectivity analysis shows that N_2 formation during NO decomposition over P25 remains approximately constant at ~23% between 70 °C and 450 °C but increases to ~30% after calcination at 600 °C, demonstrating that thermal history alters product distribution even under UV irradiation. In contrast, NO reduction in the presence of CO exhibits a decrease in N_2 selectivity from ~46% to ~25% with increasing pretreatment temperature, underscoring the competing roles of surface hydroxyls and lattice oxygen in determining reaction pathways [64].

Beyond activity metrics, TiO_2 photocatalysis is critically limited by the formation and release of NO_2, a more hazardous pollutant than NO, as reflected by substantially stricter exposure limits (The National Institute for Occupational Safety and Health (NIOSH) recommended ceiling limit: 3 ppm for NO_2 vs 25 ppm for NO), making NO_2 selectivity a decisive parameter for evaluating net environmental benefit [78, 82, 83]. As a consequence, the $DeNO_x$ index has been introduced to account for simultaneous NO removal and NO_2 generation, with several commercial TiO_2 materials exhibiting strongly negative $DeNO_x$ values despite high apparent NO conversion [62].

3.2 TiO_2-Based Photocatalysts with NO_x Storage Domains

The inability of pristine TiO_2 to suppress NO_2 release despite high UV-driven NO oxidation activity motivated the development of hybrid photocatalytic oxidation-storage architectures, in which TiO_2 provides NO oxidation functionality while secondary oxide domains, such as Al_2O_3, act as non-photocatalytic NO_x storage reservoirs [38, 84]. In TiO_2–Al_2O_3 binary systems, in-situ FTIR spectroscopy revealed that NO_2 generated on TiO_2 readily migrates to alumina domains, where it undergoes disproportionation to form surface nitrites and nitrates with substantially higher stability than those formed on TiO_2 alone [85–88]. Quantitatively, TiO_2–Al_2O_3 systems have been reported to exhibit substantially enhanced NO_x storage capacities (up to ~160% higher than Degussa P25) while simultaneously reducing NO_2(g) release by more than 50%, confirming that the improvement arises not only from increased oxidation kinetics but also from altered surface NO_x retention and storage behavior [38]. The enhanced storage performance of TiO_2–Al_2O_3 systems was attributed to the high specific surface area of γ-Al_2O_3 (200 m^2/g) and its moderate surface acidity, which favors the formation of bidentate and bridging nitrate species with intermediate adsorption strength. These findings indicate that the photocatalytic performance of binary systems is governed by the balance between NO oxidation rates on TiO_2 and the favorably highly NO_x

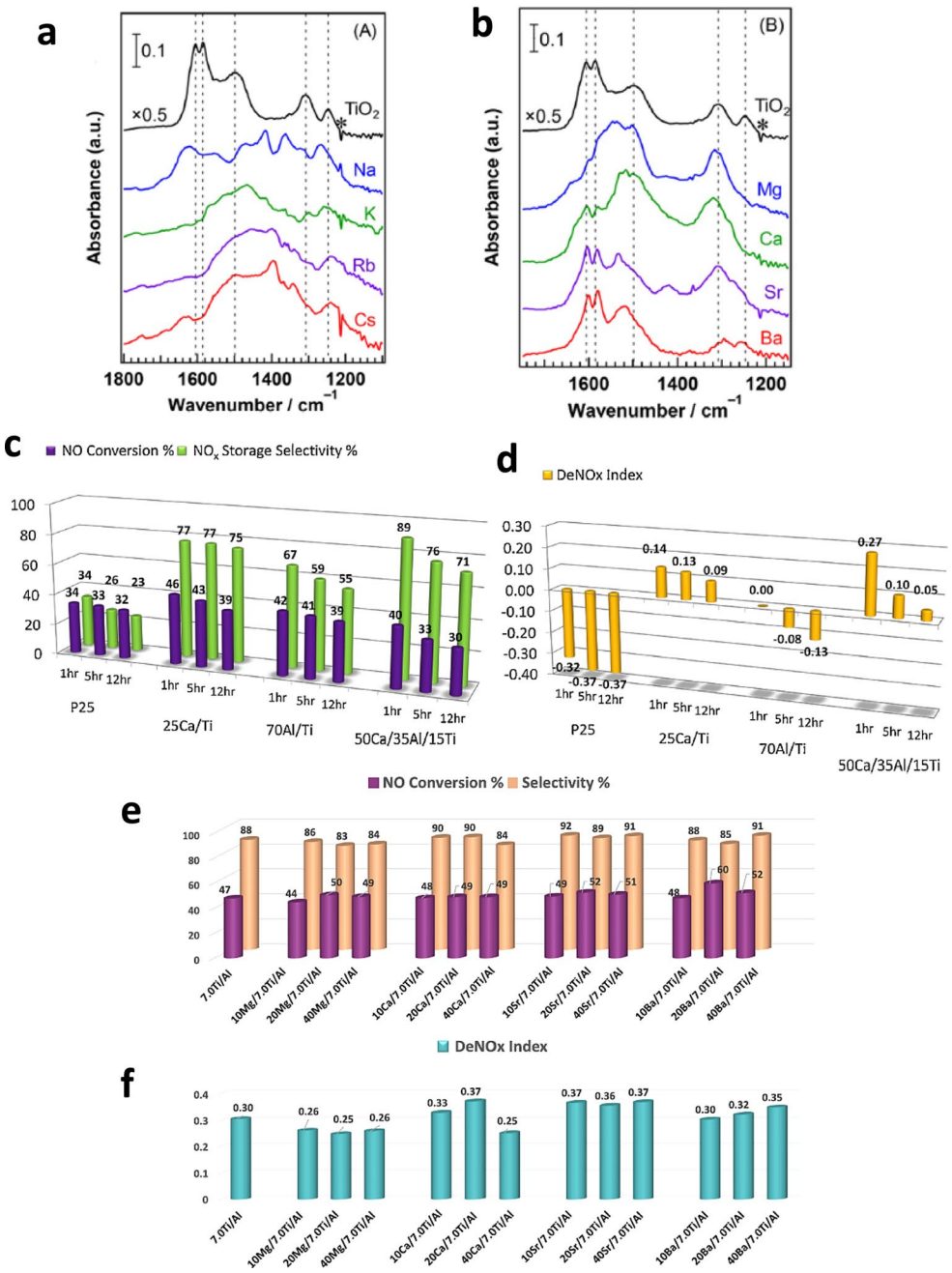

Fig. 4 Post-reaction DRIFT spectra of TiO_2 and metal-promoted TiO_2 after photocatalytic NO_x storage: **a** alkali metal-promoted TiO_2 catalysts, **b** alkaline earth metal-promoted TiO_2 catalysts [90]. Copyright, 2019, Elsevier. **c** NO(g) conversion%, NO_x storage selectivity % and **d** $DeNO_x$ index data for P25 (TiO_2), TiO_2/Al_2O_3 and CaO/TiO_2 binary mixed oxide, as well as CaO/TiO_2/Al_2O_3 ternary mixed oxide photocatalysts carried out under UV irradiation [40]. Copyright, 2020, Elsevier **e** NO(g) conversion %, NO_x storage selectivity %, **f** $DeNO_x$ index data for different MO_x/TiO_2/Al_2O_3 (M: Mg, Ca, Sr, Ba) ternary mixed oxide photocatalysts obtained after 1 h photocatalytic performance tests under UVA-light irradiation [65]. Copyright, 2024, American Chemical Society

storage capacity of alumina domains, rather than by TiO_2 activity alone [38, 57].

The acidic adsorption sites provided by γ-Al_2O_3, when complemented by alkali (Na, K, Rb, Cs) or alkaline-earth metal oxide phases (CaO, MgO, SrO, BaO) enable stronger stabilization of nitrate species, thereby enhancing the overall NO_x storage [65, 89, 90]. In-situ Diffuse Reflectance Infrared Fourier Transform Spectroscopy (DRIFTS) revealed that on bare and Ba-modified TiO_2 (Fig. 4a and 4b), NO_x is predominantly stabilized as Ti-coordinated nitrate species, evidenced by characteristic bands at 1605 and 1247 cm^{-1} (bridging), 1585 and 1308 cm^{-1} (bidentate), and 1498 cm^{-1} (monodentate), with Ba-TiO_2 exhibiting nearly identical features (1601 and 1254, 1579 and 1295, and 1519 cm^{-1}), indicating preservation of Ti-site coordination upon alkaline earth modification [90–93]. In contrast, alkali metal-modified TiO_2 (Na, K, Rb, Cs) is dominated by physically adsorbed NO_2 intermediates (1630–1690 cm^{-1}) and broad bands at 1300–1550 cm^{-1}, reflecting Ti-site blocking and weaker nitrate binding, whereas alkaline earth modification promotes strongly bound Ti-associated nitrates that govern high NO_x trapping efficiency at low temperature [90].

In the P25-based physical mixtures, CaO's extreme basicity provides strong NO_2 uptake via strong O^{2-}–Ca^{2+}

ionic interactions that stabilize NO_2^-/NO_3^- species [40]. However, CaO-rich binary mixed oxides suffer from low surface area-e.g., 25Ca/Ti shows BET specific surface area (SSA) of 39 $m^2\ g^{-1}$-so the most effective design is a ternary that combines strong CaO sites and weaker/moderate γ-Al_2O_3 sites while keeping reasonable TiO_2 content. Accordingly, the optimized 25Ca/53Al/22Ti reaches SSA 113 $m^2\ g^{-1}$ and retains a favorable (positive) $DeNO_x$ behavior after both 1 h and 12 h, while even the binary 25Ca/Ti loses its detoxification efficiency over time ($DeNO_x$ Index: +0.14 at 1 h → +0.09 at 12 h) (Fig. 4c and 4d) and generally performs best at moderate humidity (20–50% RH at 23 ± 2 °C), with high humidity being detrimental (80% RH at 23 ± 2 °C) [40]. It should be noted that CaO-based storage domains are chemically reactive under ambient conditions and may undergo hydration ($CaO \rightarrow Ca(OH)_2$) and carbonation ($CaCO_3$) in the presence of H_2O and CO_2 [94]. While such transformations can modify surface basicity and NO_x adsorption behavior, they do not necessarily result in significant material loss under mild aqueous conditions, as $Ca(OH)_2$ is only sparingly soluble. In contrast, nitrate/nitrite species (e.g., $Ca(NO_3)_2$, $Ca(NO_2)_2$) are highly water-soluble and can be removed during washing, enabling partial regeneration of storage sites [40].

In the sol–gel TiO_2/Al_2O_3 photocatalysts (7.0Ti/Al-700), adding alkaline-earth oxides by physical mixing (10, 20, or 40 wt.% MgO/CaO/SrO/BaO) further boosts NO_x storage selectivity by increasing surface basicity and creating strongly binding NO_x adsorption sites (Fig. 4e) [65]. The optimum ternary oxide formulations were reported to be 20Ca/7.0Ti/Al-700 and 20Sr/7.0Ti/Al-700, which reach a $DeNO_x$ index of +0.37 (vs. +0.30 for the unpromoted 7.0Ti/Al-700) (Fig. 4f), and the authors explicitly interpret this as a dual-site storage synergy: low-SSA, strongly binding CaO/SrO sites handle robust nitrate storage, while high SSA Al_2O_3 domains provide additional weak/moderate sites that suppress saturation of the catalyst surface with nitrates and improve longevity. It was also reported that CaO/Al_2O_3 domains also adsorb water and mitigate poisoning of TiO_2 surface due humidity at high RH values [65]. During a 12 h stability test, the 20Ca/7.0Ti/Al-700 catalyst exhibited only a moderate decrease in $DeNO_x$ index (from +0.37 to +0.28), while largely preserving its NO_x storage selectivity despite a measurable decline in NO conversion. Importantly, these measurements were conducted at an inlet NO concentration of ~1 ppm, which is significantly higher than typical urban NO levels (by approximately one order of magnitude or more). Under such realistic PHONOS operational conditions, the nitrate accumulation rate is expected to be significantly low which will result in elongation of the time required for the saturation of the NO_x-uptake capacity of the PHONOS catalyst, enabling substantial extension of the catalyst lifetime [65, 95, 96].

While the incorporation of alkali and alkaline earth metal oxides creates additional basic storage domains for nitrate stabilization, recent studies suggest that control of crystallographic surface facets of titania alone can also allow NO_x retention by modulating defect density, water adsorption, and radical formation pathways. Crystal facet engineering of brookite TiO_2 was shown to enhance photocatalytic NO_x selectivity under UV irradiation by suppressing NO_2 formation and promoting nitrate production [97]. XRD analysis revealed that brookite nanorods having (120), (111), and (121) surface facets (TALH-6U-SL) exhibited a high proportion of the (111) facet, reaching up to 68.8%. Despite having a specific surface area comparable to commercial P25 (39.9 $m^2\ g^{-1}$), TALH-6U-SL displayed a nitrate selectivity approximately 4.9 times higher than P25 and 6.8 times higher than facet-uncontrolled brookite (TALH-6U). TGA measurements showed a higher weight loss for TALH-6U-SL (3.86%) compared to TALH-6U (1.69%), indicating increased surface hydroxylation, while XPS analysis revealed a negative shift of 0.3–0.5 eV in the Ti 2p binding energies, consistent with a higher density of oxygen vacancies. Together, these structural and surface features favored enhanced water adsorption and stabilization of oxidized NO_x intermediates, leading to suppression of NO_2 release and preferential nitrate formation during photocatalytic NO oxidation [97].

Collectively, these studies establish that photocatalytic NO_x storage on TiO_2-based systems is governed by a delicate interplay between photocatalytic oxidation kinetics, surface acidity/basicity, specific surface area, and nitrate binding strength and crystallographic surface structure. From a mechanistic standpoint, efficient PHONOS catalysts must therefore integrate highly active TiO_2 oxidation sites with structurally optimized storage domains-whether with well-defined surface acidity or exposure of particular crystallographic metal oxide facets to enhance NO oxidation, strengthen nitrate retention, and minimize secondary NO_2 release while maximizing solid-state nitrate accumulation. In this context, the extent and nature of nitrate accumulation can be reliably assessed by combining quantitative analysis via ion chromatography with in-situ spectroscopic techniques such as FTIR/DRIFTS, which provide complementary insight into surface speciation and binding configurations [98, 99].

3.3 Role of Co-catalysts in TiO_2-Based PHONOS Systems

The addition of metals or metal oxides to TiO_2-based PHONOS systems as co-catalysts has been effective in

enhancing NO_x storage and selectivity. Co-catalysts have been reported to regulate the interfacial charge-transfer processes, suppress electron–hole recombination, and promote NO oxidation kinetics through modified surface redox pathways, which ultimately contribute to the stability of stored nitrate species under continuous irradiation [100–102].

Such charge-regulation effects were explicitly quantified in $Ti_{0.909}W_{0.091}O_2N_x$ under broadband irradiation conditions [101]. Photocatalytic tests showed a decrease in NO_2 concentration from 10^{-3} ppm on bare TiO_2 to below the detection limit (10^{-9} ppm), corresponding to a NO_2 suppression of more than six orders of magnitude, while nitrate selectivity increased from 29% to 90% (Fig. 5a). Spectroscopic and electrochemical analyses showed that the W^{6+}/W^{5+} redox couple functions as an electron-storage center, temporarily trapping photogenerated electrons. This stored charge enables oxygen to undergo multi-electron reduction at more positive potentials (around + 0.6 V vs RHE, where RHE refers to the reversible hydrogen electrode, a standard electrochemical reference scale) (Fig. 5b). As a result, electrons are preferentially transferred to O_2 rather than to surface-bound nitrate species, thereby suppressing their undesired back-reduction (i.e., the re-conversion of nitrate into NO_2). Electron Paramagnetic Resonance (EPR) analysis (Fig. 5c) provides direct evidence that photogenerated electrons are preferentially trapped at W^{5+} centers rather than forming Ti^{3+} species, confirming the formation of stable electron-storage sites within the $Ti_{0.909}W_{0.091}O_2N_x$ lattice. These reduced W species, characterized by low g-values indicative of strong spin–orbit coupling in 5d orbitals, demonstrate that electrons are localized at tungsten centers under irradiation [101].

For atomically dispersed Mn sites on TiO_2(B) (a metastable bronze-type (monoclinic) polymorph of TiO_2) photocatalytic experiments yielded an NO conversion of 67.15% and a $DeNO_x$ index of 58.5%, compared to 41% and 27% for pristine TiO_2(B), while NO_2 release was reduced by a factor of 2.11, indicating improved selectivity toward stored nitrate species [100]. Time-resolved photoluminescence and transient photocurrent measurements revealed prolonged charge-carrier lifetimes and increased photocurrent density for Mn-TiO_2(B), directly correlating enhanced charge separation with reduced NO_2 formation [100]. In TiO_2 rutile (R-706)-fly ash composites, the introduction of CaO and aluminosilicate-rich fly ash increased nitrate formation, as confirmed by enhanced nitrate band intensities in FTIR spectroscopy and a shift in product distribution toward NO_3^- compared to pure rutile TiO_2, despite the relatively low intrinsic NO conversion efficiency of the rutile phase (R-706) (Fig. 5d) [103]. The role of storage domains was quantified in TiO_2-Ti_3C_2-OH hybrids, where NO_x storage selectivity reached 91% and the $DeNO_x$ index increased to + 0.30 at a NO conversion of 54%, compared to a negative $DeNO_x$ on bare TiO_2, confirming that Ti_3C_2-OH acts as a strong NO_2 adsorption and hole-accepting domain (Fig. 5e-5g) [104].

These advances in interfacial engineering and storage domain design have paved the way for the development of single-atom catalysts (SACs), where metal atoms are atomically dispersed to maximize active site efficiency and metal-support interactions. Photocatalytic NO_x removal over Pd/TiO_2 (anatase/rutile mass ratio = 20.5) under UV irradiation is quantitatively governed by isolated Pd atoms rather than Pd clusters or bulk Pd species [105]. NO adsorption via in-situ DRIFTS demonstrates that the surface fraction of isolated Pd increases linearly up to 0.1 wt.% nominal Pd (0.055 wt.% surface Pd), above which Pd aggregation occurs (Fig. 6a and 6b). Representative STEM images of the 1 wt.% Pd/TiO_2 catalyst before and after NO removal are shown in Fig. 6c and 6d. The 5 h average NO_x removal efficiency scales linearly with the isolated Pd surface fraction, while photodeposited Pd nanoparticles exhibit activities comparable to bare TiO_2. Under ISO 22197-1:2007 standard conditions, flame spray pyrolysis (FSP)-made Pd/TiO_2 achieves a 4–5-fold higher NO_x removal after 5 h, with a maximum turn over number (TON_{Pd} = 65.4) at 0.1 wt.% Pd, decreasing to 7.6 at 1 wt.% Pd due to clustering. Post-reaction NO adsorption via in-situ DRIFTS confirms that nitrate species poison TiO_2 and Pd clusters, whereas the linear NO band of isolated Pd at 1847 cm^{-1} remains largely unchanged, indicating superior nitrate poisoning resistance and identifying isolated Pd atoms as the dominant active sites [105].

Vanadate single-atom-modified anatase TiO_2 calcined at 400 °C (a-TiO_2(400)-V^{SA}) shows an approximately 3-fold higher photocatalytic NO_2 conversion rate than pristine a-TiO_2(400) under simulated solar light. Whereas unmodified TiO_2 converts NO_2 exclusively to nitrate, vanadate SACs alter the product distribution, leading to partial reduction of NO_2 to NO (≈33% of converted NO_2), with nitrate remaining the dominant product. This behavior is consistent with the oxygen reduction kinetics of vanadate-SAC-modified TiO_2, where shallow intragap states associated with the V^{5+}/V^{4+} redox couple enable rapid electron extraction and fast catalytic turnover in O_2 reduction (Fig. 6e and 6f). Consequently, electron transfer from reduced vanadate sites becomes competitive with nitrate formation pathways, giving rise to reductive NO_2 conversion that is absent on pristine TiO_2 [106].

Overall, co-catalysts emerge as indispensable components in TiO_2-based PHONOS systems, not only by promoting charge separation and surface redox reactions, but also by steering NO_x oxidation pathways toward selective and stable nitrate formation.

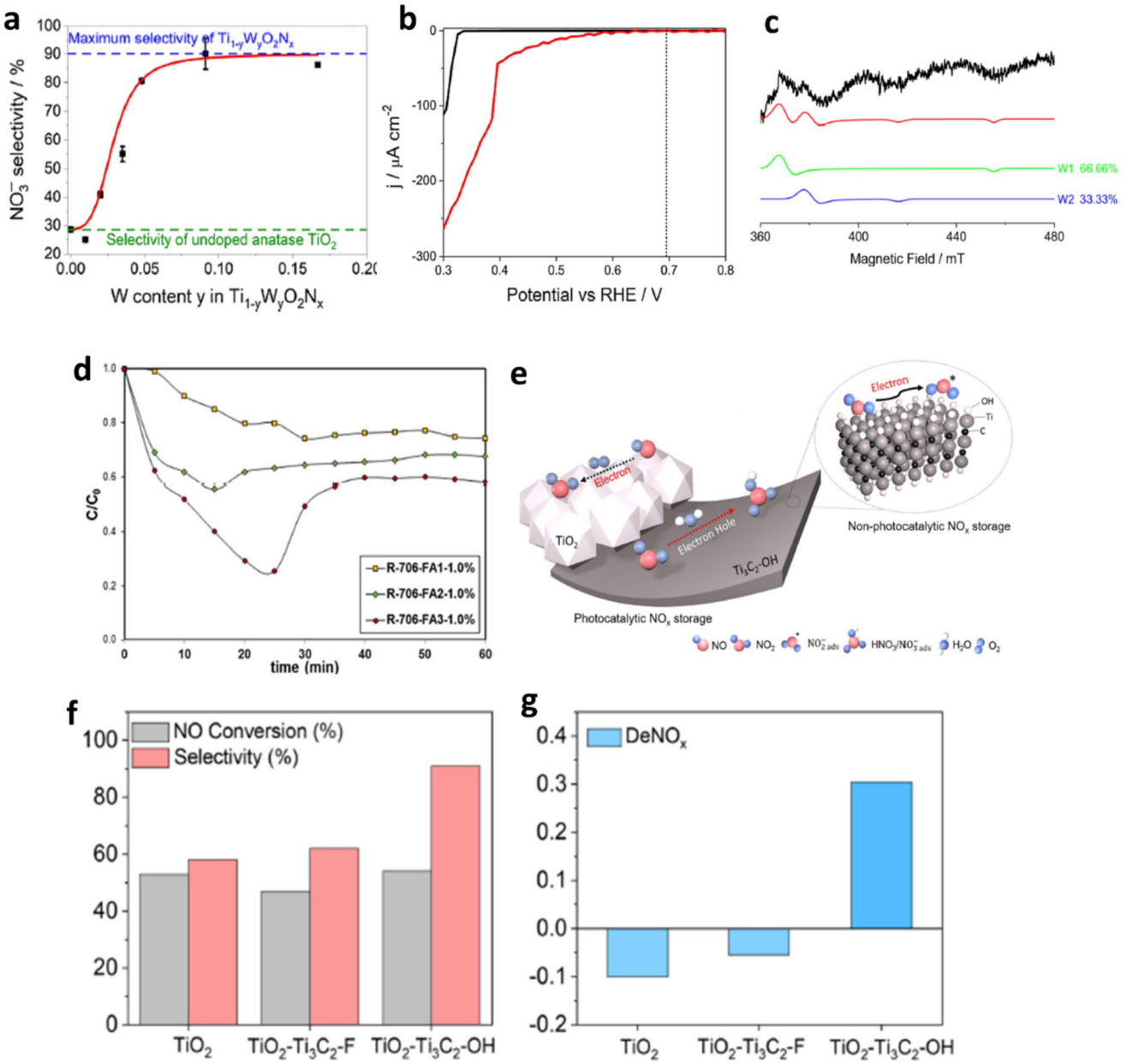

Fig. 5 **a** Selectivity of NO photocatalytic oxidation under UV/Vis irradiation with respect to nitrate (i.e., desired product) formation vs. W content y in $Ti_{1-y}W_yO_2N_x$. **b** Oxygen reduction currents vs applied potential for undoped anatase TiO_2 nanoparticles (black trace) and $Ti_{0.952}W_{0.048}O_2N_x$ (red trace). For $Ti_{0.952}W_{0.048}O_2N_x$, the potential at which ORR starts (ca. 0.6 V vs RHE) and the Tafel slope of the current profile are indicative of a two-electron-reduction process. **c** Experimental (black) and simulated (red) X-band CW EPR spectra of the $Ti_{0.909}W_{0.091}O_2N_x$ nanoparticles measured at 50 K at high fields. The simulated spectrum is deconvoluted into two components: W1 (green) and W2 (blue). The relative spectral contributions are also reported in the figure. The experimental spectrum was recorded at 100 kHz field modulation frequency, 0.2 mT field modulation amplitude, 2 μW microwave power, and 72 dB receiver gain [101]. Copyright, 2018, American Chemical Society **d** Evolution of nitric oxide concentration (initial NO conc. = 1 ppm) when TiO_2 rutile was coupled with different fly ashes (Q = 1 L min^{-1}, I = 8.2 W m^{-2}, < 0.4 ppm of H_2O, ± 2% error in the measurements of NO) [103]. Copyright, 2016, American Chemical Society. **e** Schematic illustration of NO_x abatement by TiO_2-Ti_3C_2-OH; for the sake of simplicity, the oxidation of NO to HNO_3 by photogenerated electrons and the oxidation of NO to NO_2 by photogenerated holes are not shown in the schematic. **f** NO conversion and NO_x storage selectivity and **g** $DeNO_x$ index for TiO_2, TiO_2–Ti_3C_2–F, and TiO_2–Ti_3C_2–OH [104]. Copyright, 2022, Elsevier

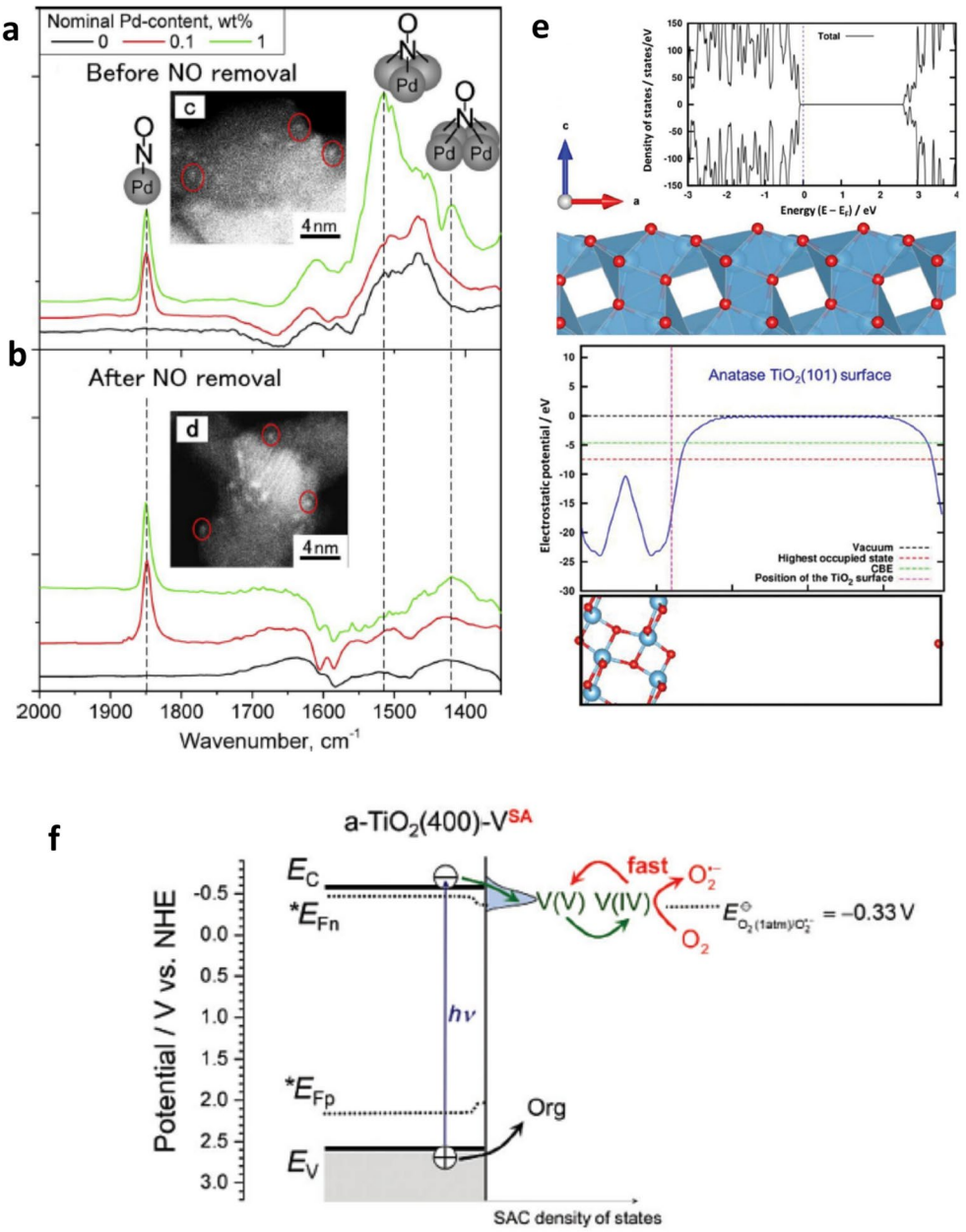

Fig. 6 DRIFT spectra of NO (1000 ppm) adsorption (after 20 min) on FSP-made Pd/TiO_2 with 0 (black), 0.1 (red) and 1 (green) wt.% Pd **a** before and **b** after NO removal. The insets show STEM images of TiO_2 with 1 wt.% Pd **c** before and **d** after NO removal. Bright spots (red circles) and gray parts show Pd subnano-clusters and TiO_2, respectively [105]. Copyright, 2018, Elsevier. **e** Periodic DFT calculations. Models of atomic structure, calculated density of states plots, and local electrostatic potential profiles of anatase TiO_2(101) surfaces with surface-grafted vanadate species. **f** Mechanism of enhancement of photocatalytic degradation rate on anatase TiO_2 surface modified with vanadate SACs. TiO_2(400)-V^{SA}, the vanadate-induced interfacial states are just below (by 0.13 eV) the conduction band edge of anatase TiO_2 (− 0.6 V vs NHE at pH 7) [106]. Ref. [106], Creative Commons CC BY license

3.4 Low-Dimensional Semiconductor Nanostructures for PHONOS Applications

Low-dimensional semiconductor nanostructures such as quantum dots (QDs), carbon quantum dots (CQDs), and quantum nanoplatelets (NPLs) have recently emerged as effective functional modifiers of TiO_2 for PHONOS, primarily by enhancing light harvesting, charge separation, and NO_2 storage selectivity [39, 107].

Functionalization of P25 (TiO_2) with thioglycolic acid (TGA)-capped CdTe quantum dots leads to a profound improvement in PHONOS performance by selectively enhancing NO_2 storage rather than merely increasing NO oxidation activity. In the TGA-capped CdTe QD-functionalized P25 system, NO conversion increased from 31% to 42–43% under UV-A and visible irradiation, while NO_x storage selectivity dramatically increased from 25-35% to as high as 92–97% (Fig. 7a). 1.0 wt.% and 2.0 wt.% CdTe/P25 stand out as the most effective compositions, delivering consistently positive $DeNO_x$ index values under both UV-A and VIS irradiation (Fig. 7b). Control experiments demonstrate that NO oxidation occurs predominantly on TiO_2 active sites, whereas the CdTe QDs and their organic capping layer facilitate downstream NO_2 adsorption and conversion to surface-bound nitrate species. This behavior is attributed to favorable band alignment (CdTe QDs direct band gap 1.96 eV), which harvest both UV and VIS-light, and promotes interfacial charge separation, suppressing

electron–hole recombination and increasing the availability of oxidative surface species required for nitrate formation, while aging studies confirm that the composite consistently outperforms bare P25 despite partial QD degradation [39]. In addition, the possible effect of temperature under VIS-light irradiation should be taken into account. Although the reactor temperature may increase upon illumination with a conventional visible light irradiation source which may also emit IR radiation (if not filtered), NO oxidation remains largely independent of temperature when normalized to the incident photon flux, indicating a predominantly photocatalytic process (Fig. 7c). In contrast, NO_x storage decreases at higher temperatures (Fig. 7d), likely due to reduced H_2O adsorption and a lower concentration of surface -OH groups required for nitrate formation. In overall, these findings indicate that the enhanced performance under VIS-light is mainly photocatalytic in origin, while elevated temperature may negatively affect NO_x storage [39].

A similar mechanistic trend is observed for the enhanced photocatalytic activity of N-doped carbon quantum dots (P25/NCQD). In this system enhanced PHONOS performance originates from interfacial electronic effects rather than structural or textural changes, as BET and XRD confirm similar surface areas and preserved anatase–rutile composition. Diffuse reflectance UV–Vis (DR-UV Vis) spectrum shows enhanced visible-light absorption with a bandgap reduction from 3.05 to 2.95 eV, consistent with Ti–O–C interfacial bond formation evidenced by FTIR and a 0.3–0.5 eV positive shift in Ti 2p XPS peaks. Consequently, P25/NCQD achieves higher NO conversion under UV (79.6%) and visible light (27%) compared to P25 (58.4% and 10%, respectively), together with improved selectivity (Fig. 7e). Reduced charge-transfer resistance observed by EIS confirms that NCQD act as efficient electron acceptors, suppressing recombination and governing NO photo-oxidation performance [108]. Although the absolute selectivity enhancement is smaller than that achieved with CdTe QDs, the results consistently indicate that zero-dimensional carbon-based sensitizers suppress electron–hole recombination and promote surface reactions leading to ionic NO_x species.

This effect becomes even more pronounced in the case of two-dimensional CdSe/CdSeTe core-crown quantum-well nanoplatelets (NPL) [107]. The core-crown NPL architecture generates a Type-II heterojunction in which photogenerated electrons are preferentially localized in the CdSe core, while holes are confined within the CdSeTe crown (Fig. 7f) [109, 110]. This spatial separation leads to the formation of long-lived, spatially indirect excitons with suppressed non-radiative recombination [111]. PL quenching observed upon NPL deposition on TiO_2 provides experimental support for efficient charge transfer from the NPLs to the TiO_2 support.

Under UV-A and visible light irradiation, the type-II band alignment promotes electron accumulation in the CdSe core and subsequent injection into the TiO_2 conduction band, while holes remain confined within the NPL phase, facilitating oxidative surface reactions. This charge carrier partitioning significantly increases the probability that photogenerated NO_2 intermediates are further oxidized and immobilized as surface nitrate species rather than desorbing into the gas phase [107]. Post-reaction XPS analysis reveals partial electronic restructuring of Cd sites following prolonged PHONOS operation, indicating that the NPL phase actively participates in interfacial charge exchange during catalysis rather than acting as a passive light absorber. Importantly, the catalyst retains superior performance relative to P25 after repeated cycles, underscoring the stability of the Type-II heterojunction strategy for practical PHONOS applications [107].

These studies demonstrate that the incorporation of low-dimensional semiconductor sensitizers into TiO_2 architectures represents a powerful strategy to overcome the intrinsic selectivity limitations of TiO_2 in PHONOS applications. Rather than maximizing NO oxidation alone, these materials enable a more balanced catalytic function by coupling efficient photo-oxidation on TiO_2 with selective NO_2 storage mediated by the sensitizer phase.

4 Visible-Light Photocatalytic Systems for NO_x Oxidation and Storage

While UV-driven PHONOS systems predominantly rely on wide-band-gap semiconductors such as TiO_2 to initiate NO oxidation and storage processes, their practical applicability is intrinsically limited by the relatively small UV photon flux of the solar spectrum. This limitation has motivated the development of visible-light-driven PHONOS systems, where band-gap engineering and the introduction of visible-light-active components enable NO_x abatement under longer-wavelength irradiation with a greater photon flux. In this context, carbon-based photocatalysts and doped TiO_2 materials have emerged as two major photocatalyst classes for extending PHONOS activity into the visible region.

4.1 Carbon-Based Photocatalysts

Carbon-based photocatalysts-most notably graphitic carbon nitride (g-C_3N_4), doped carbon frameworks, and carbon-semiconductor composites-have gained significant attention in environmental photocatalysis due to their VIS-light absorption, tunable electronic properties, and structural flexibility [112]. Unlike TiO_2, which requires UV activation, many carbonaceous photocatalysts can harvest visible

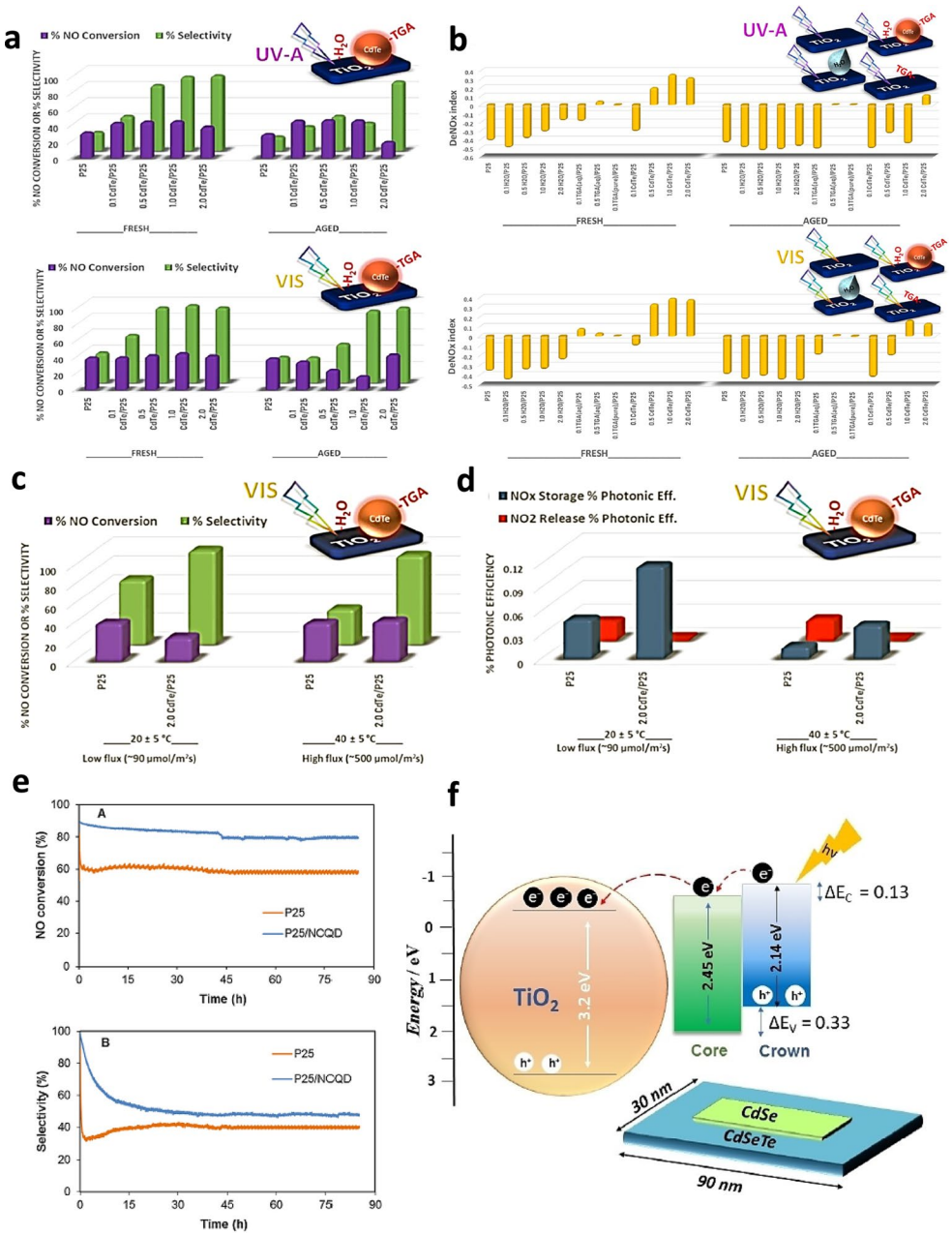

Fig. 7] **a** NO conversion and selectivity results for fresh and aged titanium dioxide (P25) and CdTe/P25 under UV-A irradiation and VIS irradiation [39]. Copyright, 2019, American Chemical Society. **b** $DeNO_x$ index results of fresh and aged titanium dioxide (P25), CdTe/P25, H_2O(l)/P25, TGA(aq)/P25, and TGA (pure)/P25 under UV-A and VIS irradiation [39]. Temperature dependent photocatalytic activity data for fresh P25 and 2.0 CdTe/P25 samples under VIS light illumination: **c** NO conversion and selectivity data vs temperature and **d** photonic efficiency vs temperature for titanium dioxide (P25) and 2.0 CdTe/P25 under VIS light [39]. **e** NO conversion (A) and selectivity (B) for P25, P25/NCQD composite during 85 h under UV radiation [108]. Copyright, 2016, Elsevier. **f** Electron energy diagram for core/crown CdSe/CdSeTe NPL on TiO_2 [107]. Copyright, 2020, Wiley

wavelengths (e.g., 400–460 nm), allowing more efficient utilization of solar irradiation. Their π-conjugated electronic structure facilitates delocalized charge transport and facilitates electron excitation under lower photon energies [113].

Among these materials, g-C_3N_4 stands out due to its moderate band gap (2.7 eV), good thermal and chemical stability, and nitrogen-rich framework enabling unique adsorption sites for NO and NO_2 [113, 114]. The layered structure of g-C_3N_4 resembles graphite, consisting of tris-triazine repeating units linked through nitrogen bridges. This structure gives rise to electron-rich lone pairs and surface Brønsted basicity, distinguishing carbon-based systems from oxide photocatalysts in their surface interactions with nitrogen oxides [115]. However, pristine g-C_3N_4 suffers from fast charge recombination, limited surface area, and suboptimal selectivity in NO oxidation [116]. These limitations have spurred extensive efforts in doping, exfoliation, heterojunction formation, mesoporous structure, and carbon-hybrid platform design [117, 118]. Template-assisted synthesis represents an effective strategy, offering fine control over the surface, electronic, and morphological features of g-C_3N_4, along with the rational design of porous frameworks [119, 120].

Photocatalytic oxidation of NO at ppb levels under visible light is intrinsically governed not only by the overall NO conversion efficiency but, more critically, by the ability

of the catalyst to suppress the formation and release of toxic NO_2 intermediates while promoting the accumulation of stable nitrate species. The collective findings of the present body of literature clearly indicate that the key challenge in g-C_3N_4-based systems lies in controlling reaction selectivity rather than simply enhancing VIS-light absorption or charge generation [117, 121, 122].

The successful incorporation of Fe_3O_4 into mpg-CN500 was confirmed by XRD analysis (Fig. 8a) [117]. Under vis-light irradiation, commercial P25 exhibits a strongly negative $DeNO_x$ index (− 0.28) due to severe NO_2 release despite moderate NO conversion. In contrast, mesoporous g-C_3N_4 calcined at 500 °C (mpg-CN500) achieves 40% NO conversion with 83% NO_x storage selectivity (Fig. 8b), resulting in a positive $DeNO_x$ index of + 0.20 (Fig. 8c). This improvement arises from its intra-band gap states, improved charge separation, and mesoporous structure facilitating gas diffusion. Further modification with 8 wt.% Fe_3O_4 improves NO_x storage selectivity to 93% and increases the $DeNO_x$ index to + 0.28, although the NO conversion decreases slightly to 35%. The $Fe^{2+/}Fe^{3+}$ redox couple promotes oxygen reduction by scavenging conduction-band electrons, thereby suppressing the reduction of surface nitrate species to NO_2 and leading to enhanced selectivity and stable multiple-cycle performance compared to bare mpg-C_3N_4 [117].

Metal-free defect engineering effectively regulates NO oxidation selectivity, as demonstrated by amorphous carbon nitride with N_{3C} vacancies (ACN3) [123]. ACN3 achieves 57.1% NO removal within 10 min with a nitrate selectivity of 86.3%, while suppressing NO_2 from 182.17 ppb on pristine g-C_3N_4 to 82.15 ppb (Fig. 8d-8f). This enhancement originates from band gap narrowing (2.58 eV) and defect-induced $n \rightarrow \pi^*$ transitions that improve visible-light absorption and charge separation, as evidenced by PL lifetimes and increased photocurrent density (70 to 130 nA cm^{-2}). DFT calculations show a pronounced decrease in the NO_2 oxidation barrier (from 2.22 eV to < 1 eV) together with strengthened O_2 adsorption at N_3C vacancy sites [123].

A similar defect-driven selectivity is observed for hierarchical porous K-doped g-C_3N_4 with nitrogen vacancies and charge transport channels (KCNN) (Fig. 9a) [124]. The optimized KCNN sample achieves a NO removal efficiency of 70.5%, outperforming pristine g-C_3N_4 (38.1%), porous g-C_3N_4 (54.5%), and solely K-doped g-C_3N_4 (58.6%), while reducing NO_2 emission by approximately 9–10% (Fig. 9b–9e). XPS analysis shows an increased C/N atomic ratio (from 0.66 to 0.70), evidencing lattice nitrogen loss and vacancy formation, whereas EPR spectra display a markedly enhanced signal intensity, confirming a higher concentration of unpaired electrons associated with N vacancies. In-situ DRIFTS reveals that NO adsorption and disproportionation occur on the KCNN surface in the dark, while visible light irradiation promotes the formation of reactive NO^+ species and the progressive conversion of NO into stable nitrate intermediates (Fig. 9f and 9g). These results demonstrate that the synergistic coexistence of nitrogen vacancies and K-induced interlayer charge transport pathways promotes efficient charge migration and ROS-driven oxidation, thereby suppressing NO_2 accumulation and enhancing NO oxidation selectivity [124].

Urea-based g-C_3N_4 (CN-U) outperforms thiourea-based g-C_3N_4 (CN-T) in Vis-light NO oxidation due to its higher surface area (137.2 vs 26.8 $m^2\ g^{-1}$), wider band gap (2.64 vs 2.47 eV), and higher nitrogen defect density [125]. In situ FT-IR demonstrates that CN-U stabilizes a broader range of N_xO_y intermediates (NO^-, $N_2O_2^{2-}$, N_2O_3, N_2O), indicating stronger defect-mediated adsorption. Enhanced charge separation in CN-U; enables higher $\cdot O_2$– and ·OH radical production, promoting rapid oxidation of intermediates into stable bidentate and bridging nitrates while suppressing monodentate nitrate accumulation. As a result, CN-U achieves higher NO removal efficiency (40.4%) than CN-T (34.9%) [125].

Surface chemistry modulation further demonstrates that selectivity can be controlled without extensive lattice reconstruction. Hydrothermally hydroxylated g-C_3N_4 (DCN-180) exhibits a NO oxidation efficiency of 65%, approximately double that of pristine DCN, while significantly reducing NO_2 concentration from 99 to 55 ppb [122]. DFT calculations confirm stronger adsorption of both NO (− 1.67 eV) and O_2 (− 0.53 eV) on hydroxylated surfaces, indicating that surface –OH groups enhance local polarization, reactant binding, and interfacial charge transfer. This approach highlights the critical role of surface modification and hydroxylation in governing NO_2 suppression [122].

The significant increase in visible-light photocatalytic NO removal performance of cyano defect- and $CaCO_3$-co-modified g-C_3N_4 (xCa-CN) (Fig. 10a) arises from the strong synergy between defect-induced electronic modulation and alkaline surface chemistry [126]. Cyano defects introduce an electron-withdrawing effect that narrows the band gap (from 2.60 to 2.49 eV) (Fig. 10b and 10c), shifts the conduction band downward, and enhances charge separation, as evidenced by a nearly tenfold increase in photocurrent density (5.38 vs 0.56 μA cm^{-2}) and reduced PL intensity. The optimal 0.5Ca-CN sample achieves a NO removal efficiency of 51.18%, significantly exceeding the performance of pristine g-C_3N_4 nanosheets (34.05%) (Fig. 10d and 10e) while simultaneously suppressing NO_2 formation by approximately 7% (Fig. 10f and 10g). Concurrently, $CaCO_3$ acts as an alkaline NO_x adsorption and trapping site, significantly increasing the adsorption energies of NO and NO_2 ($\Delta E_{ads}(NO) = -1.715$ eV; $\Delta E_{ads}(NO_2) = -1.219$ eV), transforming weak physisorption into strong chemisorption

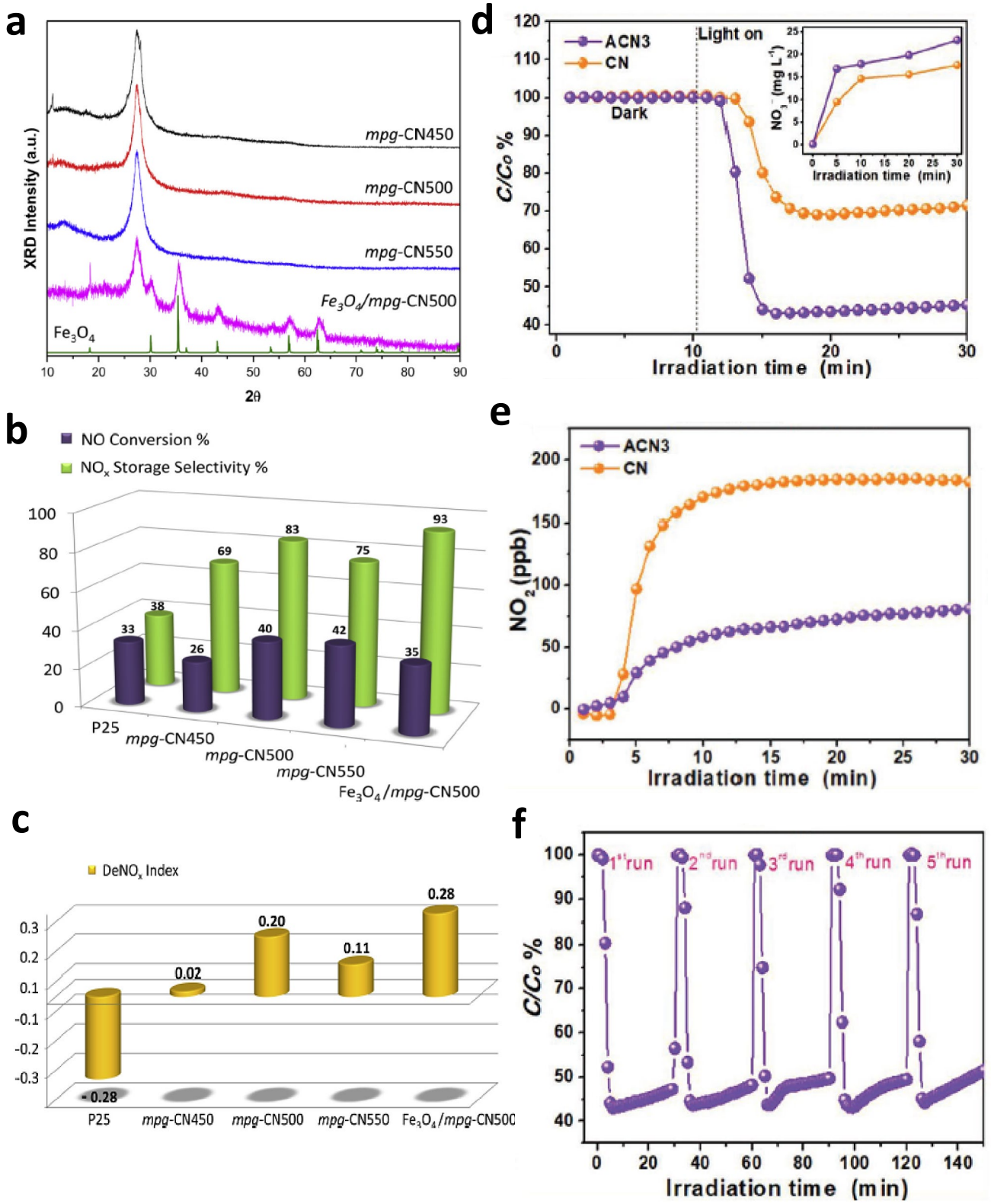

Fig. 8] **a** XRD profiles of mpg-CN450, mpg-CN500, mpg-CN550 and Fe_3O_4/mpg-CN500 photocatalysts and pure Fe_3O_4 reference material. **b** NO(g) conversion% and NO_2 storage selectivity%, **c** DeNOx index values for mpg-CN450, mpg-CN500, mpg-CN550 and Fe_3O_4/mpg-CN500 photocatalysts obtained via VIS-light irradiation [117]. Copyright, 2019, Elsevier. **d** Photocatalytic performance of CN and ACN3 samples for NO oxidation under visible light irradiation (inset shows the variation of NO_3^- concentration as a function of irradiation time). **e** NO_2 concentration as a function of irradiation time, and **f** stability test of the ACN3 photocatalyst [123]. Copyright, 2021, Wiley

and extending surface residence times. In-situ DRIFTS and DFT analyses reveal that this dual modification promotes a preferred $NO \rightarrow NO^+ \rightarrow NO_3^-$ oxidation pathway, supported by intensified ROS generation ($\cdot O_2^-$, $\cdot OH$, and $^1O_2$) and stabilization of NO^+ intermediates, thereby enabling deep oxidation while suppressing toxic NO_2 release. These results demonstrate that coupling cyano defect engineering with $CaCO_3$ surface modulation decouples activity enhancement from byproduct formation, providing a rational strategy for safe and efficient photocatalytic NO abatement under visible light [126].

The S-scheme Sb_2WO_6/g-C_3N_4 heterojunction exhibits markedly enhanced visible-light photocatalytic NO oxidation, achieving 68% NO removal from 400 ppb continuous-flow NO within 30 min for the optimal 15-Sb_2WO_6/g-C_3N_4 sample, compared with 55% for pristine g-C_3N_4, while retaining high stability over 5 cycles [127]. Band alignment analysis shows that E_{CB} values of g-C_3N_4 (− 0.84 V vs NHE) and Sb_2WO_6 (− 0.15 V vs NHE) form an S-scheme structure that selectively preserves strongly reducing electrons on g-C_3N_4 and oxidizing holes on Sb_2WO_6, leading to suppressed PL emission, enhanced photocurrent response, and reduced interfacial charge-transfer resistance. Radical trapping and in situ DRIFTS confirm an oxygen-induced NO oxidation pathway dominated by $\cdot O_2^-$, with $\cdot OH$ as a secondary species, enabling efficient conversion of NO through N_xO_y intermediates to stable nitrate products under visible-light irradiation [127].

Overall, the visible light photocatalytic behavior of g-C_3N_4 is dictated by a complex interplay between light absorption, charge-carrier dynamics, and surface redox chemistry. Rational design strategies that integrate controlled defect engineering, surface functionalization, and heterostructure construction are essential to fully exploit the potential of g-C_3N_4-based systems for efficient and selective visible-light-driven photocatalysis.

4.2 TiO_2-Based Photocatalysts

This section focuses on TiO_2-based photocatalysts designed for visible-light activation, complementing the UV-driven systems discussed in Sect. 3.3. Under visible-light irradiation, modified TiO_2 systems are commonly activated through impurity levels, defect states, or interfacial charge-transfer complexes that introduce sub-band-gap absorption [53, 128]. Non-metal doping (e.g., N, C, S), metal-ion incorporation, oxygen vacancies, and surface complexes can generate localized electronic states above the valence band or below the conduction band [59, 108]. These states enable visible-light excitation via defect-mediated transitions, however, the resulting charge carriers are often strongly localized. In contrast to carbon-based photocatalysts, visible-light-driven TiO_2 photocatalysis does not originate from intrinsic band-to-band excitation, but rather from extrinsic light-harvesting and charge-transfer mechanisms [129].

In addition to modified TiO_2 systems, Ti-based materials with alternative structural motifs, such as metal–organic frameworks (MOFs), have attracted attention for visible-light-driven photocatalysis. MIL-125(Ti) is a Ti-based MOF and thus it is not a TiO_2-based material; however, its structure contains photoactive Ti-oxo clusters that enable photocatalytic activity under visible-light irradiation [130]. In this context, the enhanced visible-light photocatalytic performance of nitrogen-doped carbon quantum dot-modified MIL-125(Ti) (N/CM(Ti)) (Fig. 11a) has been attributed to interfacial electronic interactions induced by the quantum dots, rather than structural modification of the MIL-125(Ti) framework [131]. XRD and FE-SEM confirm the preserved MOF structure, while BET analysis reveals an increased surface area from 868 to 1066 m^2g^{-1} for the optimal 2.5 vol % N/CM(Ti). XPS provides direct evidence for N–Ti–O bond formation, accompanied by a 0.4 eV negative shift in Ti 2p binding energies, indicating strong electronic interaction and modified Ti active sites (Fig. 11b). As a result, the composite achieves a NO removal efficiency of 49% under visible light, whereas pristine MIL-125(Ti) is nearly inactive. Notably, only trace NO_2 (25 ppb) is produced, and in-situ FT-IR spectra reveal the accumulation of mono- and bidentate nitrate species (1298, 1251, and 1715 cm^{-1}), demonstrating preferential oxidation and stabilization of NO_x as surface-bound nitrates (Fig. 11c and 11d). Enhanced photocurrent response (1.6-fold), reduced charge-transfer resistance, and the generation of $\cdot O_2^-$ and $\cdot OH$ radicals confirmed by EPR further indicate efficient charge separation and multi-electron NO oxidation mediated by Ti^{3+}/Ti^{4+} redox centers, collectively governing the selective PHONOS behavior of N/CM(Ti) [131].

While interfacial electronic coupling dominates in MOF-based heterostructures, similar visible-light activation in conventional TiO_2 systems can also be achieved through intrinsic defect engineering. The enhanced visible-light NO_x removal observed for oxygen-deficient, anatase-dominant TiO_2 calcined at 200 °C (TiO_2-200) primarily arises from vacancy-induced electronic modulation associated with oxygen defects [59]. XRD and Raman analyses confirm an anatase-brookite structure, while BET measurements show the highest surface area (282.7 m^2/g), favoring NO adsorption and product accumulation. UV–Vis diffuse reflectance spectra reveal extended visible-light absorption with intra band gap states, directly linked to abundant oxygen vacancies evidenced by Raman peak broadening and an EPR signal at g = 2.004. Consequently, among all as-prepared TiO_2 samples (150–500 °C) as well as commercial P25, TiO_2-200 achieves the highest NO_x conversion (53.96%) with the

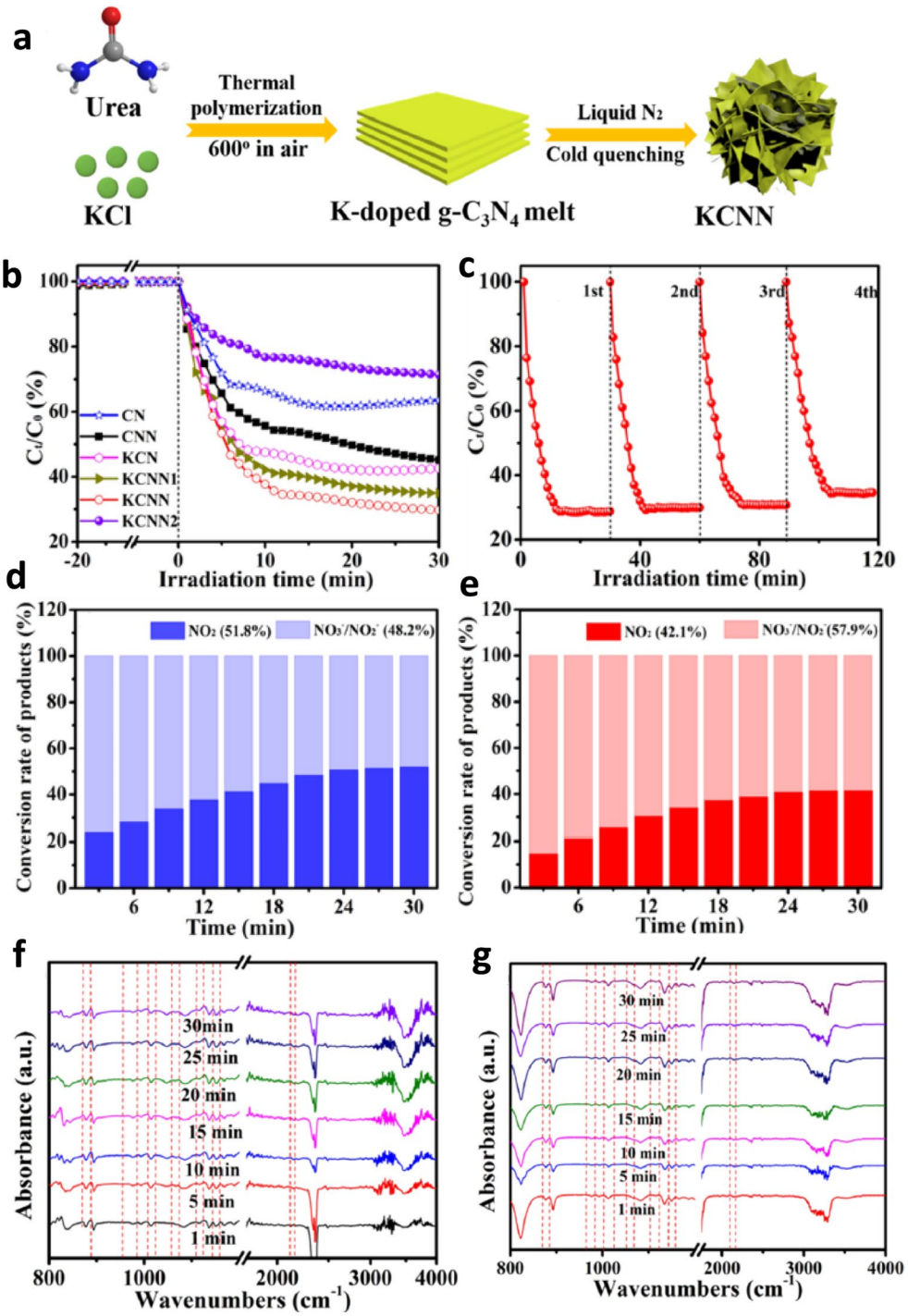

Fig. 9 **a** Schematic summarizing the synthesis procedure of KCNN photocatalyst. **b** Photocatalytic oxidation efficiencies for NO removal for various CN, CNN, KCN, and KCNN photocatalysts. **c** Cycling test of the KCNN photocatalyst; Relative intensity of conversion during 30 min of photocatalytic NO_x oxidation for **d** CN and **e** KCNN. In-situ DRIFTS data for the **f** adsorption and **g** photocatalytic oxidation of NO over KCNN photocatalyst [124]. Copyright, 2024, Elsevier

lowest NO_2 selectivity (14.92%), indicating efficient oxidation of NO_2 to surface-bound nitrate species rather than gas-phase release. Photoluminescence quenching and DFT calculations further confirm that oxygen-vacancy-induced Ti^{3+} states enhance charge separation and promote multi-electron NO oxidation, establishing defect engineering as an effective strategy for selective photocatalytic NO_x oxidation and storage [59].

Extending this concept of defect-mediated electronic modulation, atomically dispersed metal species introduce a more precisely defined strategy for tailoring charge separation and redox selectivity. Fe_1/TiO_2 hollow microspheres feature atomically dispersed Fe species anchored at surface Ti vacancies of anatase TiO_2, as confirmed by HAADF-STEM and Fe K-edge XANES/EXAFS, with average coordination numbers of 1.7 ± 0.9 Fe–Ti and 2.6 ± 0.3 Fe–O and a Fe–Ti bond length of 3.07 ± 0.07 Å, indicating surface-confined

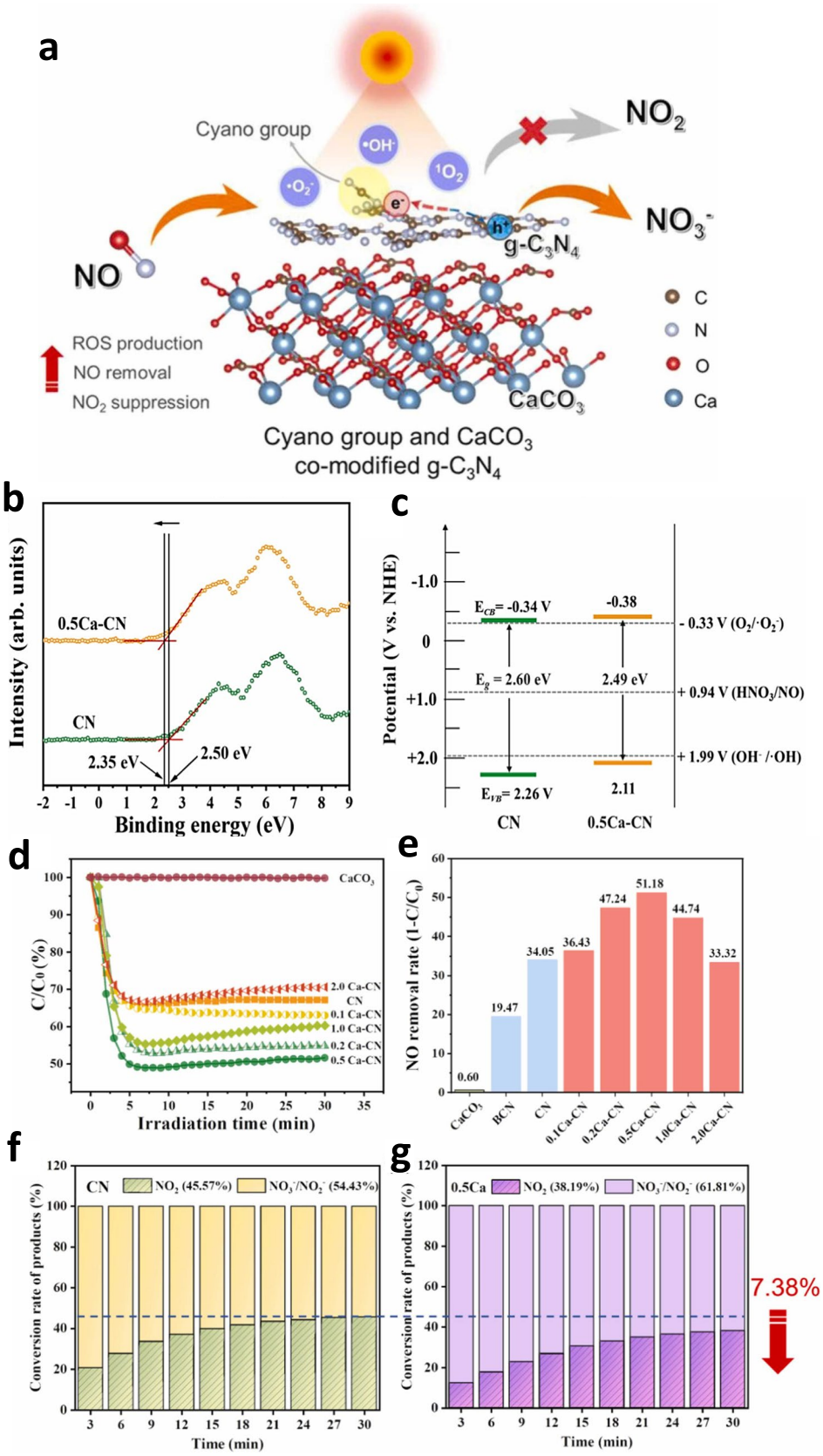

Fig. 10 **a** Proposed photocatalytic NO oxidation mechanism over xCa- CN catalysts under VIS light irradiation. **b** VB XPS spectra and **c** band structure alignments for CN and 0.5Ca-CN. **d** Relative NO concentration variation vs time for $CaCO_3$, CN and xCa-CN photocatalysts under VIS light irradiation, and **e** corresponding NO removal rates of the pristine photocatalysts. Relative product conversion rates during 30 min of photocatalytic NO_x oxidation for **f** CN and **g** 0.5Ca-CN photocatalysts [126]. Copyright, 2023, Elsevier

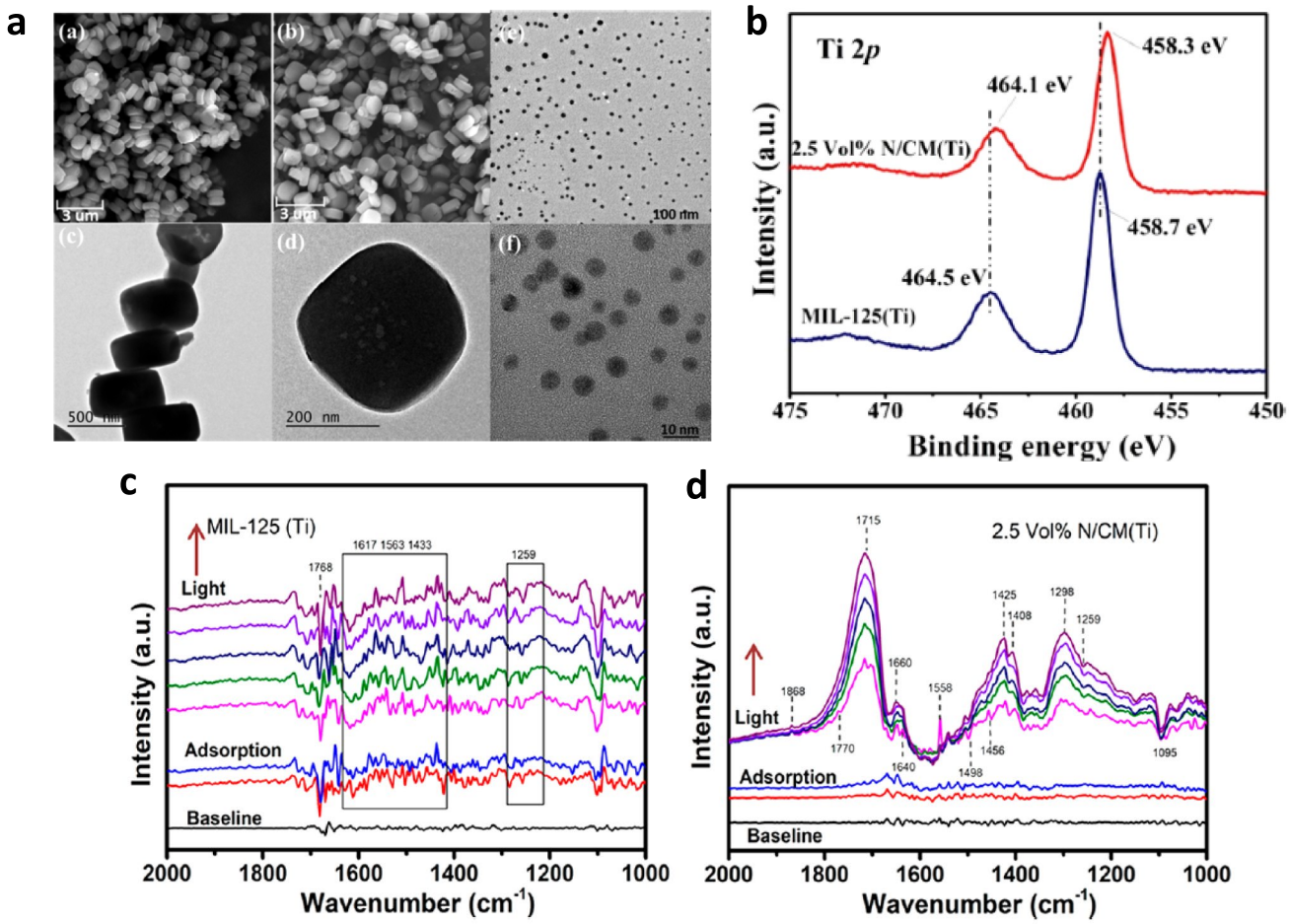

Fig. 11 **a** SEM and TEM images of the samples: (a) pure MIL-125(Ti) and (b) 2.5 vol % N/CM(Ti) photocatalysts. (c) pure MIL-125(Ti), (d) 2.5 vol % N/CM(Ti), and (e, f) N/CQDs. **b** Ti 2p XPS spectra of MIL-125(Ti) and 2.5 vol % N/CM(Ti). In-situ IR spectra of NO adsorption and VIS-light reaction of **c** MIL-125(Ti) and **d** 2.5 vol% N/CM(Ti) composite [131]. Copyright, 2020, American Chemical Society

single atoms rather than bulk doping [116, 132]. Electron transfer from Fe to neighboring Ti generates Ti^{3+} species (EPR, g = 1.992) and strongly enhances reactant adsorption: DFT calculations show that O_2 adsorption energy increases from − 0.32 to − 4.13 eV with O–O bond elongation from 1.21 to 1.40 Å, while NO preferentially binds to Fe sites with a Fe–N distance of 1.50 Å. Consequently, the optimized Fe_1/TiO_2 sample (0.58 wt.% Fe) achieves 47.91% NO removal in 30 min under visible light, compared to 20.67% for pristine TiO_2, while suppressing NO_2 formation to 1.40% selectivity (4.0 ppb). These results demonstrate that synergistic activation of NO and O_2 on single-atom Fe and adjacent Ti sites is responsible for the enhanced activity and selectivity in Fe_1/TiO_2 photocatalysts [116, 132].

5 Heterojunctions of TiO_2 and Carbon Nitride

The efficiency of photocatalytic processes is often limited by rapid charge-carrier recombination and insufficient light harvesting. The construction of heterojunction photocatalysts has been widely employed to mitigate these limitations by enhancing light harvesting, promoting spatial separation of photogenerated electron–hole pairs, and enhancing charge-transfer dynamics [133].

In heterostructured photocatalysts, the charge-transfer mechanism is fundamentally governed by the relative valence and conduction band edge positions, Fermi level equilibration, and the resulting internal electric field at the interface [133, 134]. Upon contact between two semiconductors, electron redistribution occurs until the Fermi levels align, leading to band bending and the formation of a built-in potential that drives directional charge migration. Depending on the band alignment and interfacial energetics,

different charge-transfer pathways can be established [135]. In type-II heterojunctions, photogenerated electrons and holes are spatially separated across the interface following the band edge offsets, which facilitates charge separation but often results in reduced redox potentials (Fig. 12a) [136]. In contrast, Z-scheme and S-scheme heterojunctions rely on the selective recombination of low-energy charge carriers at the interface, thereby preserving high-energy electrons and holes with strong redox capability (Fig. 12b and 12c). The S-scheme model further considers the role of internal electric fields and band bending in maintaining charge carriers with high thermodynamic driving force for redox reactions [136–138]. Therefore, the distinction between these mechanisms is not merely structural but is directly linked to the balance between charge separation efficiency and redox power, which ultimately determines photocatalytic performance.

Within this mechanistic framework, the design of heterostructured photocatalysts can be tailored to optimize both light utilization and redox performance under different irradiation conditions. UV and visible-light irradiation play complementary roles in photocatalytic NO_x removal. UV light provides high reactivity and rapid oxidation kinetics, while visible light enables the development of sustainable and energy-efficient photocatalytic systems that can be activated with higher photon fluxes [128, 140]. In this context, coupling TiO_2 with g-C_3N_4 represents a rational heterojunction design strategy to overcome the intrinsic limitations of each semiconductor by simultaneously extending visible-light absorption and modulating redox potentials [141, 142]. Such band-structure engineering is particularly critical in photocatalytic NO_x oxidation to achieve high NO_x removal while suppressing undesired NO_2 release [143].

To further illustrate the impact of band-structure engineering on photocatalytic performance, systematic variation of the initial melamine/TiO_2 weight ratio (from 3:1 to 1:7), corresponding to progressive changes in the g-C_3N_4/TiO_2 composite composition resulted in a continuous modulation of the conduction band (CB) edge from − 1.27 to − 0.67 V vs. normal hydrogen electrode (NHE) (pH 7), accompanied by a gradual widening of the band gap from 2.66 to 3.14 eV [143]. From a mechanistic standpoint, although more negative CB positions thermodynamically promote the reduction of molecular oxygen to superoxide radicals ($O_2^{-}\cdot$) excessive dilution with TiO_2 shifts the valence band (VB) toward less positive potentials, thereby constraining the oxidative conversion of NO_2 into thermodynamically stable nitrate species. This intrinsic trade-off between reduction and oxidation capability is directly manifested in photocatalytic performance. Under visible-light irradiation, the M0.2 composite (g-C_3N_4/TiO_2 = 1:4) exhibited an optimal balance, achieving 38% NO conversion with only 9% NO_2 formation, corresponding to the highest overall NO_x removal efficiency of 29%, markedly surpassing those of pristine g-C_3N_4 (1%) and TiO_2 (7%). However, this trend is not solely governed by band-edge energetics. Composites characterized by higher defect densities, as inferred from pronounced sub-band-gap absorption tails (e.g., M0.25), displayed inferior activity despite apparently favorable band edge positions, indicating that excessive defect states predominantly function as non-radiative recombination centers rather than as effective visible-light harvesting sites [143].

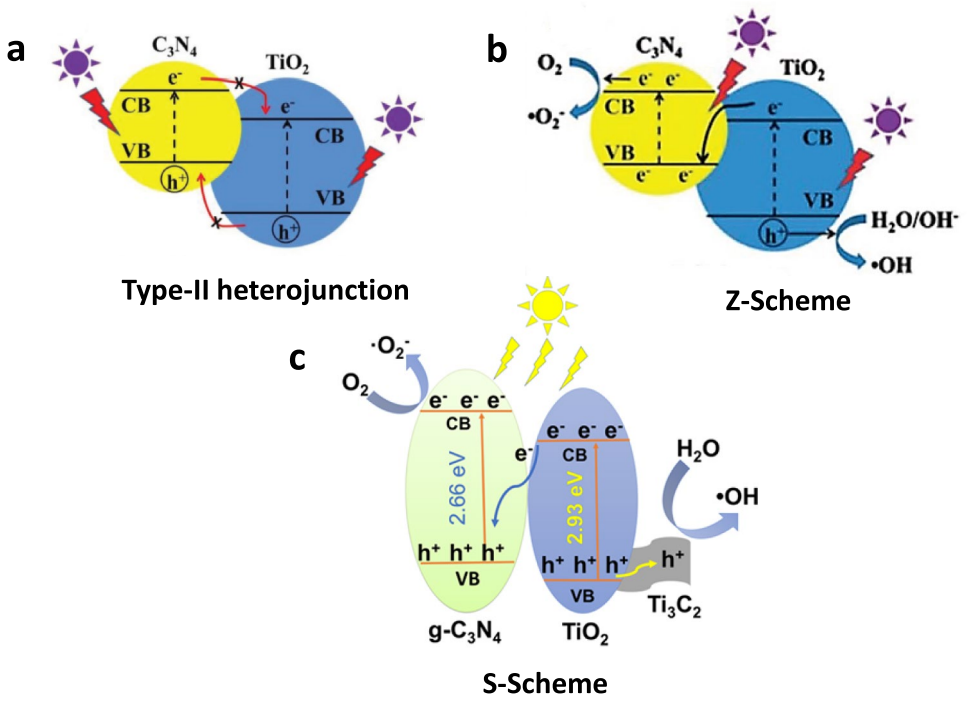

Fig. 12 Schematic illustrations of the electron–hole separation on the g-C_3N_4/TiO_2 heterojunction photocatalysts: **a** Type-II heterojunction [133], **b** direct Z-Scheme [133]. Reproduced from Ref. 133 with permission from the Royal Society of Chemistry. ; c) S-scheme in CN/TiO_2-$Ti_3C_2$450 [139]. Copyright, 2021, Elsevier.

The introduction of $CaCO_3$ provides an additional level of control by directly targeting reaction selectivity rather than photogenerated charge production. XRD, FT-IR and XPS confirmed that $CaCO_3$ is present as a crystalline calcite phase homogeneously incorporated into the g-C_3N_4/TiO_2 matrix, without altering the TiO_2 crystal structure or the optical band gap, which remains nearly unchanged (2.95–2.98 eV) [144]. Despite a reduction in BET surface area from 55.4 m^2/g (MTi0) to 48.44 m^2/g (MTi10), $CaCO_3$-modified composites exhibited a pronounced improvement in photocatalytic performance under visible light, reaching up to 18% total NO_x removal while markedly suppressing NO_2 formation. This effect is quantitatively reflected in the transition from negative to positive $DeNO_x$ index values, demonstrating that $CaCO_3$ promotes adsorption and subsequent oxidation of NO_2 into stable nitrate species through its basic surface character, thereby complementing the photoredox function of the g-C_3N_4/TiO_2 heterojunction [144].

The macroporous-mesoporous TiO_2 framework uniformly coated with g-C_3N_4 increases NO adsorption capacity (0.0060 mg/g), nearly doubling that of pristine g-C_3N_4, while facilitating charge separation via a Z-scheme interaction, as supported by reduced PL intensity and a narrowed band gap (2.71 eV) [145]. The composite achieves 34–37% NO conversion under cyan light, substantially outperforming TiO_2 and g-C_3N_4 alone, while maintaining a positive $DeNO_x$ index due to efficient conversion and retention of NO_2 as surface nitrate. These results highlight that hierarchical porosity coupled with appropriate band alignment is critical for combining activity and selectivity in NO_x photocatalysis [145].

The incorporation of partially oxidized Ti_3C_2 MXene into the g-C_3N_4/TiO_2 system establishes a well-defined S-scheme heterojunction that markedly enhances visible-light NO_x oxidation by preserving strong redox potentials and accelerating charge transfer [139]. Based on reported flat-band potentials and band structure analysis, g-C_3N_4 possesses a more negative conduction band, while TiO_2 exhibits a more positive valence band, enabling the spatial separation of reduction and oxidation sites. Upon contact, Fermi level equilibration induces band bending and an internal electric field across the g-C_3N_4/TiO_2 interface. Under visible-light irradiation, photogenerated electrons in TiO_2 recombine with holes in g-C_3N_4 at the interface, leading to the retention of high-energy electrons in g-C_3N_4 and strongly oxidizing holes in TiO_2 [139].

This charge-selection process preserves the thermodynamic driving force required for O_2 reduction to $O_2^-\cdot$ and for the subsequent oxidation of NO to nitrate species. The Ti_3C_2 MXene component, partially oxidized to form TiO_2–Ti_3C_2 interfacial domains, contributes by providing a conductive pathway that facilitates interfacial charge transfer and reduces carrier recombination, as evidenced by enhanced photocurrent response, suppressed photoluminescence, and reduced charge-transfer resistance. Importantly, the exclusion of a conventional type-II pathway is supported by the insufficient valence band potential of g-C_3N_4 for ·OH generation, indicating that the observed activity is more consistently explained by an S-scheme mechanism [139].

Collectively, recent g-C_3N_4/TiO_2 PHONOS studies indicate that the transition from NO oxidation to effective NO_x purification under visible light relies on co-designing heterojunction electronic structures with tailored adsorption and storage functionalities, emphasizing that selectivity control is as critical as photocatalytic activity in next-generation air-purification materials.

6 Experimental Methodology and Standardization in Photocatalytic NO_x Testing

The evaluation of photocatalytic NO_x oxidation performance is highly sensitive to experimental methodology, making it challenging to directly compare different studies in the absence of standardized testing conditions [146, 147]. Variations in reactor design, gas residence time, inlet NO concentration, relative humidity, and light characteristics (wavelength, intensity, and spectral distribution) have been shown to substantially influence reported NO conversion and NO_2 selectivity, even for identical photocatalyst formulations [75, 78, 148, 149]. In particular, reporting NO removal alone without quantifying NO_2 formation can lead to misleading conclusions regarding air-purification efficiency, since NO_2 contributes disproportionately to overall toxicity [78].

To address this issue, the standardized protocol defined in ISO 22197-1 establishes controlled conditions for gas flow, irradiation geometry, and simultaneous monitoring of NO and NO_2, providing a common baseline for photocatalytic performance evaluation [150]. Nevertheless, many laboratory-scale studies operate outside strict ISO 22197-1 conditions, where photon flux calibration and spectral mismatch between light sources complicate quantitative benchmarking [78]. ISO 22197-1:2016 specifies a reference method for NO removal using a flow-type reactor under controlled conditions (1 ppm NO, 3 L min^{-1} flow, 1 mW cm^{-2} UV-A irradiation, 50% RH at 25 °C) [150, 151].

The test principle is based on the continuous exposure of a test specimen to a model gas mixture containing air and NO under UV irradiation, with performance quantified by the net removal of nitrogen oxides (NO_x = NO removed − NO_2 formed); complementary dark tests are required to distinguish photocatalytic conversion from simple adsorption or

desorption. The standard mandates a well-defined experimental setup comprising a controlled gas-supply system, a UV photoreactor, and a chemiluminescence-based NO/NO_2 analyzers, with all reactor components fabricated from UV-resistant, low-adsorption materials such as glass, stainless steel, or fluoropolymers [117, 150]. Test gas preparation involves dilution of a certified NO standard (typically 30–100 µL/L) with dry or humidified air, and flow control and concentration measurements are performed on a wet-gas basis to ensure accuracy. Standardized test-piece dimensions and air-gap thickness are prescribed, along with defined procedures for sample pretreatment, adsorption, photocatalytic removal, and elution (washing) tests to assess catalyst regeneration and nitrate/nitrite balance [150]. Figure 13 shows a schematic of a flow reactor system compliant with standard testing protocols [65].

The PHONOS studies considered within the scope of this review are summarized in Table 1. As can be seen, significant variations exist among these systems in terms of light sources, reactor configurations, reaction conditions, and performance metrics, which complicate direct comparison across different PHONOS systems. This further highlights the importance of developing more standardized evaluation approaches for photocatalytic NO_x oxidation and storage.

6.1 Data Processing: Definitions of Conversion, Selectivity, and Yield

Photocatalytic performance is assessed using 3 parameters-NO conversion (%), selectivity toward NO_x storage (%), and the $DeNO_x$ index-obtained from experimental concentration vs time curves. Under the applied conditions, NO oxidation leads to two main outcomes: gaseous NO_2 formation and NO_x storage on the catalyst surface. Therefore, NO conversion (%) represents the overall oxidation activity of the material (*17*). The second parameter, selectivity (%), describes the fraction of NO oxidation products that are retained on the catalyst surface in the solid state (*18*) [40, 65].

$$\text{NO Conversion}\,(\%) = \frac{\int([\text{NO}]_{\text{in}} - [\text{NO}]_{\text{out}})\text{dt}}{\int [\text{NO}]_{\text{in}}\text{dt}}\text{x100} \tag{17}$$

$$\text{Selectivity}\,(\% - \text{towards}\,\text{NO}_x\,\text{storage}) = \frac{\int([\text{NO}_x]_{\text{in}} - [\text{NO}_x]_{\text{out}})\text{dt}}{\int([\text{NO}]_{\text{in}} - [\text{NO}]_{\text{out}})\text{dt}} \times 100 \tag{18}$$

$$\text{DeNO}_x\,\text{index} = \frac{\int([\text{NO}]_{\text{in}} - [\text{NO}]_{\text{out}})\text{dt} - 3\int([\text{NO}_2]_{\text{out}} - [\text{NO}_2]_{\text{in}})\text{dt}}{\int [\text{NO}]_{\text{in}}\text{dt}} \tag{19}$$

These calculations are based on the assumption that the conversion of gaseous NO arises exclusively from two pathways: the formation of gaseous NO_2 and the accumulation of NO_x species on the catalyst surface, while other nitrogen-containing gaseous products such as N_2O or N_2 are neglected. This assumption is justified, as photocatalytic NO oxidation predominantly yields NO_2(g) along with surface-bound species including HONO, HNO_3, and adsorbed nitrate/nitrite (NO_3^-/NO_2^-) [53]. The $DeNO_x$ index is based on the assumption that NO_2 is approximately three times more toxic than NO and was introduced to evaluate the practical relevance of photocatalytic materials [78]. A positive $DeNO_x$ value indicates an overall NO_x reduction, whereas a negative value reflects a net increase in NO_x-related toxicity. The expression given in (*19*) represents a modified form of the index originally introduced by Bloh et al. [78].

6.2 Light Sources, Photon Flux Measurement, and Quantum Efficiency

In PHONOS studies, photocatalytic NO_x oxidation has been investigated using various light sources, including UV-A lamps, metal halide lamps, filtered xenon lamps, LEDs, and

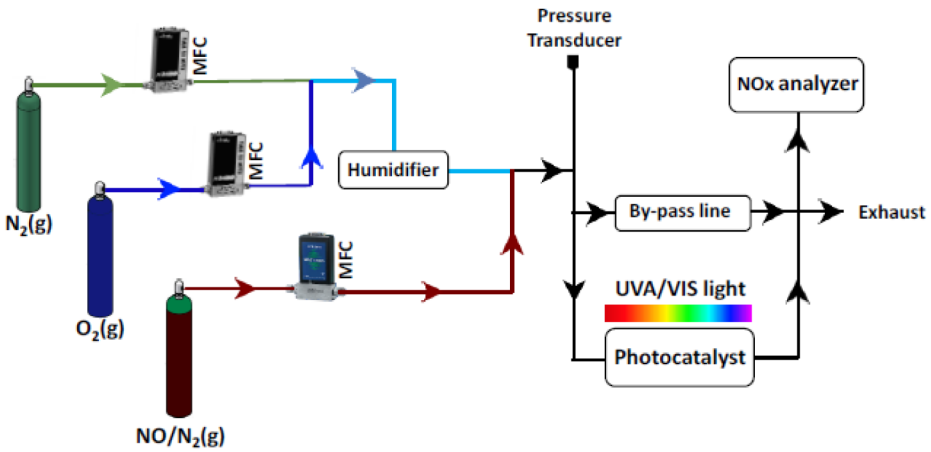

Fig. 13 Schematic description of the custom-design photocatalytic flow reactor system [65]. Copyright, 2024, American Chemical Society

Table 1 Overview of PHONOS performance across different catalysts and reaction conditions

Catalyst	Light source	Reactor type	Reaction conditions	Performance	References
TiO_2-NaOH (anatase), compared with TiO_2-C and TiO_2-1.5HNO_3 / mixed-phase TiO_2	500 W Xe lamp, 250–700 nm, 47.5 mW cm^{-2}	Continuous flow reactor; stainless steel, quartz-covered; 0.3 g powder catalyst	300 ppb NO in air, RH 20%, 800 mL min^{-1}, 25 °C	NO conv. 63.7%; NO_x conv. 53.1%; NO_2 sel. 16.06%	[80]
TiO_2-C (commercial TiO_2 reference)	500 W Xe lamp, 250–700 nm, 47.5 mW cm^{-2}	Continuous flow reactor; stainless steel, quartz-covered; 0.3 g powder catalyst	300 ppb NO in air, RH 20%, 800 mL min^{-1}, 25 °C	NO conv. 32.7%; NO_x conv. 4.8%; NO_2 sel. 82.3% (low activity, high NO_2 release)	[80]
Degussa-P25 (TiO_2)	UV, 400 W Hg lamp	Continuous-flow photoreactor; catalyst coated on borosilicate glass slide behind quartz window	909 ppm NO in Ar; total flow 5.5 cm^3 min^{-1}; decomposition and CO-assisted reduction tests; for reduction 1818 ppm CO also present	N_2 selectivity 23% (decomposition); up to 65% with CO (reduction pathway)	[64]
W/N-codoped TiO_2 and commercial TiO_2 references (P25, P90, UV100, PC50, PC105, PC500, rutile)	Ultra-Vitalux 300 W broadband lamp; photon flux 5.268×10^{-5} mol s^{-1} m^{-2}	Glass flow-through reactor; powder on glass frit; irradiated through optical window	8 ppm NO in synthetic air, RH 42%, 27 °C, flow rate 8.33×10^{-7} m^3 s^{-1}	Selectivity strongly dependent on composition; up to 82–91% nitrate selectivity at high W loadings	[78]
TiO_2/Al_2O_3 (binary oxide, P1/P2)	UVA (350–368 nm)	Flow reactor	1 ppm NO, 70% RH	Up to 176% higher NO_x removal and 75% lower NO_2 emission vs P25	[57]
M-TiO_2 (Ba, Cs modified)	UV (360 nm)	Fixed-bed quartz reactor	200 ppm NO, 3% O_2	NSC up to 187 µmol g^{-1} (enhanced NO_x trapping)	[90]
TiO_2-CaO-Al_2O_3	UVA (315–400 nm)	Packed bed flow reactor (ISO-type, PMMA holder, online NO_x detection)	1 ppm NO, 50% RH	Improved NO_x removal vs P25 ($DeNO_x$ metrics)	[40]
MO_x/TiO_2/Al_2O_3 (CaO-promoted)	UVA	Packed bed flow reactor (ISO-type)	1 ppm NO, 50% RH	NO conv. 52%, NO_x storage selectivity 86%, $DeNO_x$ index + 0.30	[65]
$Ti_{0.909}W_{0.091}O_2N_x$	UV–vis irradiation (band gap 3.17 eV + vis absorption)	Continuous flow photoreactor	NO_x in air (ppm level, humid conditions)	Improved nitrate selectivity via enhanced O_2 reduction pathways (multi-electron transfer)	[101]
TiO_2 (rutile) + fly ash (1 wt%)	UV (fluorescent lamps, 8.2 W m^{-2})	Continuous flow reactor (ISO-type)	1 ppm NO, air, ambient	Up to 67% NO removal; enhanced nitrate formation vs bare rutile	[103]
TiO_2-Ti_3C_2-OH (MXene hybrid)	UV (320 nm, 2 mW cm^{-2})	Continuous flow reactor (ISO-type, quartz window)	1 ppm NO, 50% RH	NO conversion 54%; NO_x storage selectivity 91%; $DeNO_x$ index + 0.30	[104]
Pd/TiO_2 (single-atom Pd)	Solar light (100 mW cm^{-2})	Continuous flow reactor (ISO standard)	1 ppm NO, 50% RH	3–4 × higher NO removal vs TiO_2; suppressed NO_2 formation; enhanced nitrate selectivity	[105]
CdTe QDs/P25 TiO_2	UV-A (7.7–8.3 W m^{-2}, 315–400 nm); Vis (450–500 µmol m^{-2} s^{-1}, 400–700 nm)	Continuous flow photoreactor (ISO-type)	1 ppm NO, 50% RH	NO conv.: 42% (UV), 43% (vis); selectivity: 92–97%	[39]
CdSe/CdSeTe NPL/P25	UV-A (8 W m^{-2}); Vis (450–500 µmol m^{-2} s^{-1}	Continuous flow photoreactor (ISO-type)	1 ppm NO, controlled RH	Enhanced selectivity vs P25	[107]
N-doped carbon QDs/TiO_2 (P25/NCQD)	UV-A (365 nm); Vis	Continuous flow reactor (Pyrex window)	1 ppm NO, 50% RH, 25 °C	NO conv. 27% (vis) vs 10% P25; selectivity increases	[108]
Fe_3O_4/mpg-C_3N_4	Visible (450–500 µmol m^{-2} s^{-1}, 400–700 nm)	Continuous flow photoreactor (ISO-type)	1 ppm NO, 50% RH	NO conv. 35%, NO_x storage selectivity 93%, $DeNO_x$ index + 0.28	[117]

Table 1 (continued)

Catalyst	Light source	Reactor type	Reaction conditions	Performance	References
Amorphous carbon nitride (ACN, N3C vacancies)	Visible light	Flow reactor	Ppm-level NO	NO removal: 57.1%; selectivity 86%	[123]
Hierarchical porous g-C_3N_4 (K-doped, N vacancies, KCNN)	Visible LED (30 W)	Continuous flow photoreactor (film-type)	500 ppb NO, 50% RH, 25 °C	NO removal: 70.5% (vs 38.1% bulk g-C_3N_4)	[124]
Defective g-C_3N_4 (CN-U)	Visible light (150 W halogen lamp)	Continuous flow reactor (4.5 L, quartz window)	625 μg m^{-3} NO	NO removal: 40.4% (vs 34.9% for CN-T)	[125]
Hydroxylated g-C_3N_4 (DCN-180)	Visible LED (λ≥420 nm)	Continuous flow reactor	ppm-level NO, air	NO removal: 65.0% (vs 32.5% pristine DCN)	[122]
Cyano-defect + $CaCO_3$ modified g-C_3N_4 (0.5Ca-CN)	Visible LED (λ>420 nm)	Continuous flow reactor (4.5 L)	550 ppb NO, air	51.18% NO removal (vs 34.05% pristine CN)	[126]
Sb_2WO_6/g-C_3N_4 (S-scheme, 15%)	Visible light (Xe lamp)	Continuous flow reactor (quartz-covered)	400 ppb NO, air	NO removal > 68% (30 min)	[127]
Oxygen-deficient TiO_2 (TiO_2-200)	Visible (420–700 nm, 35.8 mW cm^{-2} Xe lamp)	Continuous flow reactor (114 cm^3, quartz-covered)	400 ppb NO, 55% RH, air	NO conv.: 70% NO_2 selectivity: 14.9%	[59]
N/CQD-MIL-125(Ti) (2.5 vol%)	Visible (λ>420 nm, Xe lamp)	Continuous flow reactor (4.5 L)	420 ppb NO, air flow	NO removal 49%	[131]
Fe_1/TiO_2 hollow microspheres (SAC)	Visible light	Flow photoreactor	ppm-level NO in air	Enhanced NO oxidation + suppressed NO_2 formation	[132]
g-C_3N_4/TiO_2 + $CaCO_3$	UV-A (Philips Cleo Compact 15 W, 10 W m^{-2}) / Visible (Nordex T5-8W-4000 K, 7000 lx)	Continuous flow reactor (ISO-type)	1 ppm NO, 50% RH	NO_x removal quantified; strong suppression of NO_2 release	[144]
g-C_3N_4/TiO_2 composites (ratio-dependent)	UV and visible	Flow reactor (ISO-type)	1 ppm NO, 50% RH	NO and NO_x removal efficiencies evaluated; optimal at 1:4 ratio (highest activity)	[143]
Hierarchical TiO_2-g-C_3N_4 (Z-scheme, macro-mesoporous)	Cyan light (blue + green)	Continuous flow reactor (ISO-type, laminar flow, quartz window)	1 ppm NO, 50% RH, air	NO con.: 34–37%; DeNOx index: + 74 ppm	[145]
g-C_3N_4/TiO_2/Ti_3C_2 MXene (S-scheme)	Visible (λ>420 nm, Xe lamp)	Flow reactor	500 ppb NO, 50% RH	NO removal: 66.3%; low NO_2 generation; stable over multiple cycles	[139]

solar simulators (AM 1.5 G = 1 SUN), each differing significantly in spectral distribution and photon flux [65, 117, 131, 152]. Since photocatalytic reactions are governed by the number of photons interacting with the catalyst rather than by lamp power alone, photon flux normalization and photonic (quantum) efficiency analysis (Eq. *20* and *21*) are essential for meaningful comparison across different light sources. Photon flux is commonly determined using chemical actinometry or calibrated radiometric measurements combined with spectral information of the light source. Its accurate determination is crucial, as photocatalytic activity depends on the number of incident photons rather than nominal light power, and photon-flux-normalized metrics enable reliable comparison across different irradiation conditions and reactor configurations [78, 153]. Normalizing activity to photon flux allows intrinsic catalytic performance to be distinguished from artifacts arising from wavelength mismatch or intensity variations, particularly in selectivity-sensitive NO_x purification systems [128, 154]. For visible-light-driven systems, additional parameters such as photon flux distribution, spectral power density, and sample temperature should be carefully recorded [129].

$$\mathrm{NO_x\ storage\ \%\ Photonic\ efficiency}\ (\xi) = \frac{\mathrm{n(NO_x\ stored\ on\ the\ catalyst\ surface)}}{\mathrm{n\ (photon)}} \times 100 \tag{20}$$

$$\mathrm{NO_2\ release\ \%\ Photonic\ efficiency}\ (\xi) = \frac{\mathrm{n\ (NO_2\ released\ to\ the\ atmosphere)}}{\mathrm{n\ (photon)}} \times 100 \tag{21}$$

where n (photon) is defined as:

$$\mathrm{n\ (photon)} = \frac{(\mathrm{I} \times \lambda \times \mathrm{A} \times \mathrm{t})}{(\mathrm{N_A} \times \mathrm{h} \times \mathrm{c})} \tag{22}$$

I: photon power density of lamp, λ: mean emission wavelength of the lamp, A: the surface area of the photocatalyst exposed to light irradiation; t represents the duration of the

performance test, t: duration of the performance test, N_A: Avogadro number, h: Plank constant, c: speed of light

The photonic efficiency values defined in Eqs. (*20*) and (*21*) represent the percentage of stored solid-state NO_x species (or released gaseous NO_2) relative to the number of photons incident on the catalyst surface during a 60 min photocatalytic test [65].

6.3 Reactor Design and Optical Geometry

Photocatalytic NO_x oxidation has been studied using several reactor configurations, with planar (flat/flat plate) reactor geometries reactors being the most common laboratory setup, typically operated at gas flow rates of 1–3 L min^{-1}, residence times of 1–5 s, and UV-A irradiances in the range of 5–20 W m^{-2} [150]. Although their simple geometry facilitates comparison, flat-bed reactors frequently exhibit irradiance non-uniformities exceeding ± 20–30% across the catalyst surface, leading to diffusion-limited regions and edge effects that distort apparent kinetics [44]. Annular reactors, where light is introduced radially, can achieve more homogeneous photon distribution and higher optical utilization efficiencies, but reported light attenuation along the axial direction can exceed 40%, depending on catalyst coating thickness and lamp geometry [155].

Monolithic (honeycomb) reactors, widely used in automotive catalysis, offer geometric surface areas up to 500–1000 m^2 m^{-3} and realistic laminar flow patterns, yet variations in channel diameter (typically 1–4 mm) and coating loadings strongly affect mass transfer and light penetration, limiting quantitative comparison between studies [66, 147]. In contrast, packed-bed or particle-based reactors are rarely employed for gas-phase NO_x photocatalysis because external mass-transfer limitations dominate at gas velocities above 0.1–0.2 m/s, and optical shielding significantly reduces effective photon absorption [146]. Across all reactor types, accurate interpretation of photocatalytic performance critically depends on reliable optical characterization, as discrepancies in reported NO conversion and NO_2 selectivity are frequently linked to poorly defined irradiance values, unreported lamp-to-sample distances, and the absence of photon-flux-normalized metrics [78, 153].

6.4 Role of Humidity and Water Layer Thickness

Adsorbed molecular water and its decomposition products (H^+, ·OH, OH^-) can exert a promoting or inhibitory effect on photocatalytic $DeNO_x$ reactions depending on the reaction conditions [156]. Upon photon absorption, the formation of electron–hole (e^-–h^+) pairs on the TiO_2 surface leads to two main reaction pathways: hole-driven pathways initiated by the decomposition of surface-adsorbed water to form reactive ·OH species, and electron-driven pathways resulting from O_2 adsorption followed by superoxide (O_2^-·) formation [65]. During PHONOS, nitrogen in NO is oxidized from the + 2 to higher oxidation states (+ 3 to + 5), forming NO_2^-, NO_2, and NO_3^- species; this makes the overall process highly dependent on the hole population on the surface. Consequently, the accumulation of hole-binding species such as negatively charged surface hydroxides can enhance charge recombination and suppress photocatalytic activity. Furthermore, under high relative humidity conditions, excess surface water can reduce NO conversion by promoting non-photocatalytic nitrite and nitrate decomposition or by consuming ·OH radicals through hydrogen peroxide formation, thus decreasing the efficiency of NO_x oxidation [40, 149].

The effect of humidity on PHONOS was systematically investigated by varying the relative humidity between 30% and 80% for TiO_2/Al_2O_3-based mixed metal oxide photocatalysts [65]. At low to moderate relative humidity levels (30–50% at 23 ± 2 °C), all studied photocatalysts (P25, 7.0Ti/Al-700, and 20Ca/7.0Ti/Al-700) exhibited high NO conversion and NO_2 storage selectivity, indicating that the presence of adsorbed water was sufficient to initiate photocatalytic $DeNO_x$ pathways without blocking active sites. In contrast, at high relative humidity (80% RH at 23 ± 2 °C), both NO conversion and NO_x storage selectivity decreased significantly, which was attributed to competitive adsorption of molecular water on TiO_2 active sites and the formation of bridging hydroxide (OH_b) species acting as hole scavengers. The negative impact of high humidity was markedly less pronounced for CaO-promoted catalysts, as CaO domains served as preferential water adsorption sites, limiting hydroxide accumulation on photoactive TiO_2 domains. Additionally, disordered AlO_x regions were shown to function as sacrificial water adsorption sites, further mitigating humidity-induced deactivation [65].

6.5 Flow Rate and Residence Time Effects

Gas flow rate directly controls the residence time of NO within photocatalytic reactors and therefore governs the extent of adsorption, surface reaction, and NO_x storage during PHONOS operation [76]. Experimental studies on TiO_2-based systems demonstrate that decreasing residence time leads to lower NO conversion due to kinetically incomplete oxidation, as NO molecules desorb before sequential oxidation to nitrite and nitrate species can occur. Transient and steady-state kinetic measurements reveal that NO conversion increases with residence time only up to a critical threshold of approximately 10–12 s, beyond which conversion plateaus, indicating an equilibrium-limited regime rather than continued kinetic enhancement [77].

This plateau behavior confirms that extended contact time alone cannot indefinitely improve PHONOS performance, as surface nitrate accumulation progressively limits the availability of photoactive sites [77]. Rigorous kinetic modeling performed under ISO 22197-1 conditions further shows that at high flow rates, PHONOS systems transition from reaction-controlled to transport-influenced regimes, where gas-phase residence time becomes shorter than the characteristic surface reaction time [76, 150]. Computational Fluid Dynamics (CFD)-assisted analyses indicate that even under nominal plug-flow conditions, variations in local residence time can significantly influence apparent NO conversion, emphasizing that flow rate effects must be decoupled from intrinsic photocatalyst activity [76]. From an application perspective, indoor air purification studies consistently report that excessive flow rates reduce effective NO_x removal efficiency, whereas extremely long residence times offer diminishing returns due to nitrate saturation and secondary deactivation phenomena [147]. Together, these results demonstrate that PHONOS efficiency is maximized within a narrow residence-time window, where surface reaction kinetics, NO_x storage capacity, and mass transport are optimally balanced.

6.6 Quantitative Estimation of Nitrate Accumulation under Representative PHONOS Conditions

The amount of NO_x (i.e., nitrate) species accumulated on the catalyst surface under representative operating conditions provides a useful indication of whether nitrate build-up is likely to become a limiting factor in PHONOS systems. A rough estimate can be obtained using a simple molar balance. The inlet molar flow rate of NO ($n_{NO,in}$) can be written as;

$$n_{NO,in}\,(\mathrm{mol/h}) = y_{NO} x\, n_{tot}\,(\mathrm{mol/h}) \quad (23)$$

and the total molar flow rate (n_{tot}) of inlet gas mixture is;

$$n_{tot}\,(\mathrm{mol/h}) = V/V_m \quad (24)$$

where y_{NO} is the NO(g) mole fraction, V is the volumetric flow rate (L h^{-1}) of inlet gas mixture, and V_m = 24.465 L mol^{-1} is the molar volume of an ideal gas at 25 °C and 1 atm.

For typical PHONOS catalytic tests carried out at atmospheric pressure (i.e., 1 atm), the inlet NO(g) concentration is 1 ppm, the total inlet gas mixture ($NO(g)+O_2(g)+N_2(g)$) flow rate, V, is 12.250 sccm (i.e., 0.01225 L min^{-1}), the catalyst mass is 200 mg, and the reaction time is 1 h. One can assume that an optimized PHONOS system can operate with 52% NO conversion and 86% NO_x storage selectivity under 50% RH at 25 °C [65]. Then, for such a PHONOS system, n_{tot} can be estimated to be 0.01225 L min^{-1} / 24.465 L mol^{-1} = 5.01×10^{-4} mol min^{-1}. For an inlet NO(g) concentration of 1 ppm, the corresponding NO(g) mole fraction is $y_{NO} = 1 \times 10^{-6}$. Thus, $n_{NO,in} = 5.01 \times 10^{-10}$ mol min^{-1} = 0.0301 µmol h^{-1}. Using the estimated NO conversion of 52%, the amount of NO converted per hour ($n_{NO,conv.}$) to adsorbed nitrate, nitrite or gaseous NO_2 can be estimated to be $n_{NO,conv.} = 0.52 \times 0.0301$ µmol h^{-1} = 0.0157 µmol h^{-1}. If 86% of the converted NO is stored as nitrate species, the NO_x accumulation rate on the catalyst surface can be estimated to be $n_{NOx,stored} = 0.86 \times 0.0157$ µmol h^{-1} = 0.0135 µmol h^{-1}. For a catalyst mass of 0.200 g, this corresponds to 0.0135 µmol h^{-1} / 0.200 g = 0.0675 µmol g_{cat}^{-1} h^{-1} of NO_x storage per hour per gram of catalyst. Thus, under the typical PHONOS experimental conditions, the estimated specific NO_x accumulation (storage) rate on the catalyst surface is estimated to be approximately 0.0675 µmol g_{cat}^{-1} after 1 h.

A conventional NSR catalyst (e.g., $Pt/BaO/Al_2O_3$ operating at 300 °C) exhibits typical total NO_x storage capacities on the order of 150 µmol g_{cat}^{-1} after complete saturation of the NSR catalyst with adsorbed NO_x species during the lean phase [157]. In contrast, under typical PHONOS conditions, the NO_x accumulation rate on the PHONOS catalyst is estimated to be only 0.0675 µmol g^{-1} h^{-1}. Thus, unlike NSR catalytic systems used in automobile NO_x emission control systems which can reach NO_x storage saturation within minutes due to the high NO(g) concentration levels produced by the internal combustion engines, requiring frequent regeneration; in the case of PHONOS catalytic systems significantly lower NO(g) concentrations in the atmosphere enable prolonged continuous operation of PHONOS systems (i.e., presumably for many days) without a need for frequent regeneration.

7 Conclusion

Photocatalytic NO_x oxidation and storage (PHONOS) represents a uniquely promising strategy for mitigating low-concentration, distributed NO_x emissions under ambient conditions using renewable solar energy in a sustainable manner. Yet, despite the maturity of TiO_2-based photocatalysis and the expanding library of carbonaceous and hybrid materials, the mechanistic complexity of NO oxidation, the challenge of achieving high nitrate selectivity, and the instability of nitrate under fluctuating environmental conditions continue to constrain large-scale adoption.

A critical insight emerging from the literature is that photocatalytic NO_x removal is not a single-step oxidation

reaction, but a coupled oxidation-storage-release process governed by surface chemistry, environmental parameters, and catalyst architecture. Effective catalyst design must therefore simultaneously address;

i. Charge separation and reactive oxygen species generation for rapid NO oxidation,
ii. Controlled radical and protonation chemistry to suppress HONO/NO_2 release,
iii. Stable nitrate binding under variable humidity, and
iv. Long-term resistance to photochemical and environmental degradation.

Equally essential is methodological rigor. Without standardized gas compositions, humidity control, photon-flux measurements, and unified selectivity metrics, mechanistic insights and performance evaluations remain fragmented. Establishing robust international testing protocols, alongside the development of visible light responsive catalysts, single atom systems, and durable heterojunction architectures will be central to enabling photocatalytic NO_x oxidation and storage to transition from laboratory demonstrations to impactful urban environmental technologies.

By integrating mechanistic understanding, material innovation, and standardized evaluation, the field is poised to deliver next-generation photocatalysts capable of providing safe, efficient, and sustainable NO_x removal in real atmospheric environments.

Acknowledgements The authors gratefully acknowledge Miray Tamer for valuable scientific discussions and insightful comments.

Author Contributions R.B.T and E.O. wrote the main manuscript text. R.B.T. prepared all figures. All authors reviewed and edited the manuscript. All authors have given approval to the final version of the manuscript.

Funding Open access funding provided by Bilkent University.

Data Availability No datasets were generated or analysed during the current study.

Declarations

Conflict of interest The authors declare no competing interests.

Methods of Using Artificial Intelligence (Ai) Tools During the writing of some parts of this review, the authors utilized assistance from an Ai tool (i.e., ChatGPT, OpenAI, 2026) for correcting grammatical, spelling errors, and improving the readability of the text. In the preparation of several sections, summaries of the existing work in the literature were generated by the Ai tool. These summaries were manually edited and modified by the authors and the personalized relevant parts of these summaries were incorporated into the text. Authors carefully reviewed all Ai generated output and made corrections where necessary to ensure scientific accuracy.

References

1. Angelo J, Andrade L, Madeira LM, Mendes A (2013) An overview of photocatalysis phenomena applied to NO_x abatement. J Environ Manage 129:522–539. https://doi.org/10.1016/j.jenvman.2013.08.006
2. Liu YX, Liu L, Wang Y (2021) A critical review on removal of gaseous pollutants using sulfate radical-based advanced oxidation technologies. Environ Sci Technol 55(14):9691–9710. https://doi.org/10.1021/acs.est.1c01531
3. Orellano P, Reynoso J, Quaranta N, Bardach A, Ciapponi A (2020) Short-term exposure to particulate matter (PM10 and PM2.5), nitrogen dioxide (NO2), and ozone (O3) and all-cause and cause-specific mortality: systematic review and meta-analysis. Environ Int. https://doi.org/10.1016/j.envint.2020.105876
4. Huangfu P, Atkinson R (2020) Long-term exposure to NO_2 and O_3 and all-cause and respiratory mortality: a systematic review and meta-analysis. Environ Int. https://doi.org/10.1016/j.envint.2020.105998
5. World Health Organization (2021) WHO global air quality guidelines. Particulate matter (PM2.5 and PM10), ozone, nitrogen dioxide, sulfur dioxide and carbon monoxide. Geneva: World Health Organization; 2021. Licence: CC BY-NC-SA 3.0 IGO.
6. Air Quality download service for verified and Up To Date data, 2013-now, European Environment Agency (EEA). https://www.eea.europa.eu/en/analysis/publications/air-quality-status-report-2025/nitrogen-dioxide
7. Emissions Database for Global Atmospheric Research, Global Air Pollutant Emissions. https://edgar.jrc.ec.europa.eu/dataset_ap81
8. Leverett J, Lie WH, Khan MHA, Ma ZP, Daiyan R, Amal R (2025) Navigating the challenges of global NO emissions throughout the energy transition: state of play and outlook. Sustain Energ Fuels 9(14):3780–3790. https://doi.org/10.1039/d4se01806k
9. Crippa M, Guizzardi D, Pagani F, Schiavina M, Melchiorri M, Pisoni E, Graziosi F, Muntean M, Maes J, Dijkstra L, Van Damme M, Clarisse L, Coheur P (2024) Insights into the spatial distribution of global, national, and subnational greenhouse gas emissions in the Emissions Database for Global Atmospheric Research (EDGAR v8.0). Earth Syst Sci Data 16(6):2811–2830. https://doi.org/10.5194/essd-16-2811-2024
10. Roy S, Baiker A (2009) NO_x storage-reduction catalysis: from mechanism and materials properties to storage-reduction performance. Chem Rev 109(9):4054–4091. https://doi.org/10.1021/cr800496f
11. Garin F (2001) Mechanism of NO_x decomposition. Appl Catal A Gen 222(1–2):183–219. https://doi.org/10.1016/S0926-860x(01)00827-4
12. Roy S, Hegde MS, Madras G (2009) Catalysis for NOx abatement. Appl Energ 86(11):2283–2297. https://doi.org/10.1016/j.apenergy.2009.03.022

13. Say Z, Mihai O, Kurt M, Olsson L, Ozensoy E (2019) Trade-off between NO_x storage capacity and sulfur tolerance on Al_2O_3/ZrO_2/TiO_2–based $DeNO_x$ catalysts. Catal Today 320:152–164. https://doi.org/10.1016/j.cattod.2018.01.028
14. Hu Z, Wan CZ, Lui YK, Dettling J, Steger JJ (1996) Design of a novel Pd three-way catalyst: integration of catalytic functions in three dimensions. Catal Today 30(1–3):83–89. https://doi.org/10.1016/0920-5861(95)00332-0
15. Liu G, Gao PX (2011) A review of NO storage/reduction catalysts: mechanism, materials and degradation studies. Catal Sci Technol 1(4):552–568. https://doi.org/10.1039/c1cy00007a
16. Matsumoto S (1996) DeNO(x) catalyst for automotive lean-burn engine. Catal Today 29(1–4):43–45. https://doi.org/10.1016/0920-5861(95)00259-6
17. Ozensoy E, Hess C, Goodman DW (2004) Understanding the catalytic conversion of automobile exhaust emissions using model catalysts: CO+NO reaction on Pd(111). Top Catal 28(1–4):13–23. https://doi.org/10.1023/B:TOCA.0000024330.71495.b1
18. Schlatter JC, Mitchell PJ (1979) Three-way catalyst response to transients. Ind Eng Chem Prod Res Dev 19:293–298
19. Shelef M, Graham GW (1994) Why rhodium in automotive three-way catalysts? Catal Rev 36(3):433–457. https://doi.org/10.1080/01614949408009468
20. Takahashi N, Shinjoh H, Iijima T, Suzuki T, Yamazaki K, Yokota K, Suzuki H, Miyoshi N, Matsumoto S, Tanizawa T, Tanaka T, Tateishi S, Kasahara K (1996) The new concept 3-way catalyst for automotive lean-burn engine: NO_x storage and reduction catalyst. Catal Today 27(1–2):63–69. https://doi.org/10.1016/0920-5861(95)00173-5
21. Takeuchi M, Matsumoto S (2004) NO storage-reduction catalysts for gasoline engines. Top Catal 28(1–4):151–156. https://doi.org/10.1023/B:TOCA.0000024344.91688.e4
22. Tsinoglou DN, Weilenmann M (2009) A simplified three-way catalyst model for transient hot-mode driving cycles. Ind Eng Chem Res 48(4):1772–1785. https://doi.org/10.1021/ie8010325
23. Wu CH, Hammerle RH (1983) Development of a low cost, thermally stable, monolithic three-way catalyst system. Ind Eng Chem Prod Res Dev 22:559–565
24. Yamagata H (2005) The catalyst. Sci Technol Mater Automotive Engines. https://doi.org/10.1533/9781845690854.228
25. Yoshida T, Sato A, Suzuki H, Tanabe T, Takahashi N (2006) Development of high performance three-way-catalyst. SAE Technical Papers
26. Kayhan E, Andonova SM, Sentürk GS, Chusuei CC, Ozensoy E (2010) Fe promoted NO_x storage materials: structural properties and NO_x uptake. J Phys Chem C 114(1):357–369. https://doi.org/10.1021/jp907982q
27. Chen R, Zhang TS, Guo YQ, Wang JW, Wei JX, Yu QJ (2021) Recent advances in simultaneous removal of SO_2 and NO_x from exhaust gases: removal process, mechanism and kinetics. Chem Eng J. https://doi.org/10.1016/j.cej.2020.127588
28. Bao JJ, Mao L, Zhang YH, Fang HM, Shi YJ, Yang LJ, Yang HM (2016) Effect of selective catalytic reduction system on fine particle emission characteristics. Energ Fuel 30(2):1325–1334. https://doi.org/10.1021/acs.energyfuels.5b02029
29. Busca G, Lietti L, Ramis G, Berti F (1998) Chemical and mechanistic aspects of the selective catalytic reduction of NO_x by ammonia over oxide catalysts: a review. Appl Catal B Environ Energy 18(1–2):1–36. https://doi.org/10.1016/S0926-3373(98)00040-X
30. Guo MY, Lis B, Ford ME, Wachs IE (2022) The effect of non-redox promoters (AlO_x, PO_x, SiO_x and ZrO_x) and surface sulfates on supported V_2O_5-WO_3/TiO_2 catalysts in selective catalytic reduction of NO with NH_3. Appl Catal B Environ Energy. https://doi.org/10.1016/j.apcatb.2022.121128
31. Heck RM, Farrauto RJ (2001) Automobile exhaust catalysts. Appl Catal A Gen 221(1–2):443–457. https://doi.org/10.1016/S0926-860x(01)00818-3
32. Ngo AB, Vuong TH, Atia H, Weiss J, Rabeah J, Armbruster U, Brückner A (2022) Role of V and W sites in V_2O_5-WO_3/TiO_2 catalysts and effect of formaldehyde during NH_3-SCR of NO_x. ChemCatChem. https://doi.org/10.1002/cctc.202200175
33. Nova I, Tronconi E (2014) Urea-SCR technology for deNOx after treatment of diesel exhausts, vol 5. Springer, New York
34. Pinoy LJ, Hosten LH (1993) Experimental and kinetic modelling study of $DeNO_x$ on an industrial V_2O_5-WO_3/TiO_2 catalyst. Catal Today 17(1–2):151–158. https://doi.org/10.1016/0920-5861(93)80018-V
35. Skaf Z, Aliyev T, Shead L, Steffen T (2014) The state of the art in selective catalytic reduction control. SAE Tech Papers. https://doi.org/10.4271/2014-01-1533
36. Han LP, Cai SX, Gao M, Hasegawa J, Wang PL, Zhang JP, Shi LY, Zhang DS (2019) Selective catalytic reduction of NO_x with NH_3 by using novel catalysts: state of the art and future prospects. Chem Rev 119(19):10916–10976. https://doi.org/10.1021/acs.chemrev.9b00202
37. Kumar MS, Alphin MS, Kumar PS, Raja S (2023) A review on zeolite catalyst for $deNO_x$ performance in ammonia-selective catalytic reduction. Fuel. https://doi.org/10.1016/j.fuel.2022.126828
38. Soylu AM, Polat M, Erdogan DA, Say Z, Yildirim C, Birer Ö, Ozensoy E (2014) TiO_2–Al_2O_3 binary mixed oxide surfaces for photocatalytic NO_x abatement. Appl Surf Sci 318:142–149. https://doi.org/10.1016/j.apsusc.2014.02.065
39. Leinen MB, Dede D, Khan MU, Çaglayan M, Koçak Y, Demir HV, Ozensoy E (2019) CdTe quantum dot-functionalized P25 titania composite with enhanced photocatalytic NO_2 storage selectivity under UV and Vis irradiation. Acs Appl Mater Inter 11(1):865–879. https://doi.org/10.1021/acsami.8b18036
40. Çaglayan M, Irfan M, Ercan KE, Kocak Y, Ozensoy E (2020) Enhancement of photocatalytic NO abatement on titania additional metal oxide NO -storage domains: interplay between surface acidity, specific surface area, and humidity. Appl Catal B Environ. https://doi.org/10.1016/j.apcatb.2019.118227
41. He F, Jeon W, Choi W (2021) Photocatalytic air purification mimicking the self-cleaning process of the atmosphere. Nat Commun 12(1):2528. https://doi.org/10.1038/s41467-021-22839-0
42. Levy H 2nd (1971) Normal atmosphere: large radical and formaldehyde concentrations predicted. Science 173(3992):141–143. https://doi.org/10.1126/science.173.3992.141
43. Finlayson-Pitts BJ, Pitts JN Jr (1997) Tropospheric air pollution:ozone, airborne toxics, polycyclic aromatichydrocarbons, and particles. Science 276(5315):1045–1051. https://doi.org/10.1126/science.276.5315.1045
44. Fujishima A, Zhang XT, Tryk DA (2008) TiO_2 photocatalysis and related surface phenomena. Surf Sci Rep 63(12):515–582. https://doi.org/10.1016/j.surfrep.2008.10.001
45. Fujishima A, Honda K (1972) Electrochemical photolysis of water at a semiconductor electrode. Nature 238(5358):37–38
46. Fujishima A, Rao TN, Tryk DA (2000) Titanium dioxide photocatalysis. J Photochem Photobiol C Photochem Rev 1(1):1–21. https://doi.org/10.1016/S1389-5567(00)00002-2
47. Fujishima AHK, Watanabe T (1999) TiO_2 photocatalysis: fundamentals and applications. BKC Inc, Japan
48. Schneider J, Matsuoka M, Takeuchi M, Zhang JL, Horiuchi Y, Anpo M, Bahnemann DW (2014) Understanding TiO_2 photocatalysis: mechanisms and materials. Chem Rev 114(19):9919–9986. https://doi.org/10.1021/cr5001892
49. Folli A, Campbell SB, Anderson JA, Macphee DE (2011) Role of TiO_2 surface hydration on NO oxidation photo-activity. J Photoch Photobio A 220(2–3):85–93. https://doi.org/10.1016/j.jphotochem.2011.03.017

50. Ibusuki T, Takeuchi K (1994) Removal of low concentration nitrogen-oxides through photoassisted heterogeneous catalysis. J Mol Catal 88(1):93–102. https://doi.org/10.1016/0304-5102(93)E0247-E
51. Negishi N, Takeuchi K, Ibusuki T (1997) The surface structure of titanium dioxide thin film photocatalyst. Appl Surf Sci 121:417–420. https://doi.org/10.1016/S0169-4332(97)00349-8
52. Lewis RJ, NJNY S (1996) Sax's dangerous properties of industrial materials. N Y 3:1928
53. Freitag J, Domínguez A, Niehaus TA, Hülsewig A, Dillert R, Frauenheim T, Bahnemann DW (2015) Nitrogen(II) oxide charge transfer complexes on TiO2: a new source for visible-light activity. J Phys Chem C 119(9):4488–4501. https://doi.org/10.1021/jp5108069
54. Song M, Zhao XX, Liu PF, Mu JC, He GZ, Zhang CL, Tong SR, Xue CY, Zhao XJ, Ge MF, Mu YJ (2023) Atmospheric NO_x oxidation as major sources for nitrous acid (HONO). Npj Clim Atmos Sci. https://doi.org/10.1038/s41612-023-00357-8
55. Epling WS, Campbell LE, Yezerets A, Currier NW, Parks JE (2004) Overview of the fundamental reactions and degradation mechanisms of NO_x storage/reduction catalysts. Catal Rev 46(2):163–245. https://doi.org/10.1081/Cr-200031932
56. Cheng L, Ge QF (2008) Effect of BaO morphology on NO_x abatement: NO_2 interaction with unsupported and γ-Al_2O_3-supported BaO. J Phys Chem C 112(43):16924–16931. https://doi.org/10.1021/jp806884c
57. Polat M, Soylu AM, Erdogan DA, Erguven H, Vovk EI, Ozensoy E (2015) Influence of the sol-gel preparation method on the photocatalytic NO oxidation performance of TiO_2/Al_2O_3 binary oxides. Catal Today 241:25–32. https://doi.org/10.1016/j.cattod.2014.04.001
58. Yang L, Hakki A, Wang F, Macphee DE (2017) Different roles of water in photocatalytic DeNOx mechanisms on TiO(2): basis for engineering nitrate selectivity? ACS Appl Mater Interfaces 9(20):17034–17041. https://doi.org/10.1021/acsami.7b01989
59. Ma JZ, Wu HM, Liu YC, He H (2014) Photocatalytic removal of NO_x over visible light responsive oxygen-deficient TiO. J Phys Chem C 118(14):7434–7441. https://doi.org/10.1021/jp500116n
60. Djurisic AB, Leung YH, Ng AMC (2014) Strategies for improving the efficiency of semiconductor metal oxide photocatalysis. Mater Horizons 1(4):400–410. https://doi.org/10.1039/c4mh00031e
61. Wu ZB, Sheng ZY, Liu Y, Wang HQ, Tang N, Wang J (2009) Characterization and activity of Pd-modified TiO_2 catalysts for photocatalytic oxidation of NO in gas phase. J Hazard Mater 164(2–3):542–548. https://doi.org/10.1016/j.jhazmat.2008.08.028
62. Lasek J, Yu YH, Wu JCS (2013) Removal of NO_x by photocatalytic processes. J Photoch Photobio C 14:29–52. https://doi.org/10.1016/j.jphotochemrev.2012.08.002
63. Xue T, Li J, Chen LC, Li KL, Hua Y, Yang Y, Dong F (2024) Photocatalytic NO_x removal and recovery: progress, challenges and future perspectives. Chem Sci 15(24):9026–9046. https://doi.org/10.1039/d4sc01891e
64. Bowering N, Walker GS, Harrison PG (2006) Photocatalytic decomposition and reduction reactions of nitric oxide over Degussa P25. Appl Catal B Environ Energy 62(3–4):208–216. https://doi.org/10.1016/j.apcatb.2005.07.014
65. Ebrahimi E, Irfan M, Kocak Y, Rostas AM, Erdem E (2024) Origins of the photocatalytic NO_x oxidation and storage selectivity of mixed metal oxide photocatalysts: prevalence of electron-mediated routes, surface area, and basicity. J Phys Chem C 128(4):1669–1684. https://doi.org/10.1021/acs.jpcc.3c07634
66. Boyjoo Y, Sun HQ, Liu J, Pareek VK, Wang SB (2017) A review on photocatalysis for air treatment: from catalyst development to reactor design. Chem Eng J 310:537–559. https://doi.org/10.1016/j.cej.2016.06.090
67. Cant NW, Cole JR (1992) Photocatalysis of the Reaction between ammonia and nitric-oxide on TiO_2 surfaces. J Catal 134(1):317–330. https://doi.org/10.1016/0021-9517(92)90231-6
68. Courbon H, Pichat P (1984) Room-temperature interaction of $N^{18}O$ with ultraviolet-illuminated titanium-dioxide. J Chem Soc Farad T 80:3175–3185. https://doi.org/10.1039/f19848003175
69. Lu WG, Olaitan AD, Brantley MR, Zekavat B, Erdogan DA, Ozensoy E, Solouki T (2016) Photocatalytic conversion of nitric oxide on titanium dioxide: cryotrapping of reaction products for online monitoring by mass spectrometry. J Phys Chem C 120(15):8056–8067. https://doi.org/10.1021/acs.jpcc.5b10631
70. Linsebigler AL, Lu GQ, Yates JT (1995) Photocatalysis on TiO_2 surfaces—principles, mechanisms, and selected results. Chem Rev 95(3):735–758. https://doi.org/10.1021/cr00035a013
71. Wu XJ, Van Waeyenberg J, Vangestel D, Sels B (2025) The overlooked solvent effects: a reconsideration of the paradigm in semiconductor photocatalysis. Energ Environ Sci 18(3):1191–1204. https://doi.org/10.1039/d4ee04157g
72. Kamat PV (2012) Manipulation of charge transfer across semiconductor interface. A criterion that cannot be ignored in photocatalyst design. J Phys Chem Lett 3(5):663–672. https://doi.org/10.1021/jz201629p
73. Hashimoto K, Irie H, Fujishima A (2005) TiO_2 photocatalysis: a historical overview and future prospects. Jpn J Appl Phys 44(12):8269–8285. https://doi.org/10.1143/Jjap.44.8269
74. Abdelfattah I, El-Shamy AM (2024) A comparative study for optimizing photocatalytic activity of TiO_2-based composites with ZrO_2, ZnO, Ta_2O_5, SnO, Fe_2O_3, and CuO additives. Sci Rep UK. https://doi.org/10.1038/s41598-024-77752-5
75. Mills A, Andrews R, Han R, O'Rourke C, Hodgen S (2020) Supersensitive test of photocatalytic activity based on ISO 22197-1:2016 for the removal of NO. J Photoch Photobio A. https://doi.org/10.1016/j.jphotochem.2020.112734
76. Muñoz V, Casado C, Suárez S, Sánchez B, Marugán J (2019) Photocatalytic NOx removal: rigorous kinetic modelling and ISO standard reactor simulation. Catal Today 326:82–93. https://doi.org/10.1016/j.cattod.2018.09.001
77. Devahasdin S, Fan C Jr, Li KY, Chen DH (2003) TiO_2 photocatalytic oxidation of nitric oxide: transient behavior and reaction kinetics. J Photoch Photobio A 156(1–3):161–170. https://doi.org/10.1016/S1010-6030(03)00005-4
78. Bloh JZ, Folli A, Macphee DE (2014) Photocatalytic NO_x abatement: why the selectivity matters. Rsc Adv 4(86):45726–45734. https://doi.org/10.1039/c4ra07916g
79. Langhammer D, Kullgren J, Österlund L (2022) Adsorption and oxidation of NO_2 on anatase TiO_2: concerted nitrate interaction and photon-stimulated reaction. Acs Catal 12(16):10472–10481. https://doi.org/10.1021/acscatal.2c03334
80. Wang AJ, Wu QQ, Han C, Yang H, Xue XX (2021) Significant influences of crystal structures on photocatalytic removal of NO_x by TiO_2. J Photoch Photobio A. https://doi.org/10.1016/j.jphotochem.2020.113020
81. Dalton JS, Janes PA, Jones NG, Nicholson JA, Hallam KR, Allen GC (2002) Photocatalytic oxidation of NO_x gases using TiO_2: a surface spectroscopic approach. Environ Pollut 120(2):415–422. https://doi.org/10.1016/S0269-7491(02)00107-0
82. Luttrell WE (2014) Nitrogen dioxide. J Chem Health Saf 21(2):28–30. https://doi.org/10.1016/j.jchas.2014.01.008
83. National Institute for Occupational Safety and Health (NIOSH) Pocket guide to chemical hazards: nitrogen dioxide.
84. Hoffmann MR, Martin ST, Choi WY, Bahnemann DW (1995) Environmental applications of semiconductor photocatalysis. Chem Rev 95(1):69–96. https://doi.org/10.1021/cr00033a004
85. Ozensoy E, Peden CHF, Szanyi J (2006) Model NOx storage systems: Storage capacity and thermal aging of BaO/θ-Al_2O_3/

NiAl(100). J Catal 243(1):149–157. https://doi.org/10.1016/j.jcat.2006.06.028
86. Andonova SM, Sentürk GS, Kayhan E, Ozensoy E (2009) Nature of the Ti–Ba interactions on the BaO/TiO_2/Al_2O_3 NO_x storage system. J Phys Chem C 113(25):11014–11026. https://doi.org/10.1021/jp9005026
87. Sentürk GS, Vovk EI, Zaikovskii VI, Say Z, Soylu AM, Bukhtiyarov VI, Ozensoy E (2012) SOx uptake and release properties of TiO_2/Al_2O_3 and BaO/TiO_2/Al_2O_3 mixed oxide systems as NO_x storage materials. Catal Today 184(1):54–71. https://doi.org/10.1016/j.cattod.2011.12.006
88. Ozensoy E, Peden CHF, Szanyi J (2005) NO_2 adsorption on ultrathin θ-Al2O3 films: formation of nitrite and nitrate species. J Phys Chem B 109(33):15977–15984. https://doi.org/10.1021/jp052053e
89. Hummatov R, Gülseren O, Ozensoy E, Toffoli D, Üstünel H (2012) First-Principles investigation of NO_x and SO_x adsorption on anatase-supported BaO and Pt overlayers. J Phys Chem C 116(10):6191–6199. https://doi.org/10.1021/jp208790a
90. Tamai K, Hosokawa S, Asakura H, Teramura K, Tanaka T (2019) Low-temperature NO_x trapping on alkali or alkaline earth metal modified TiO_2 photocatalyst. Catal Today 332:76–82. https://doi.org/10.1016/j.cattod.2018.07.045
91. Kantcheva MM, Bushev VP, Hadjiivanov KI (1992) Nitrogen-dioxide adsorption on deuteroxylated titania (anatase). J Chem Soc Faraday T 88(20):3087–3089. https://doi.org/10.1039/ft9928803087
92. Ramis GG, Busca G, Lorenzelli V, Forzatti P (1990) Fourier-transform infrared study of the adsorption and coadsorption of nitric-oxide, nitrogen-dioxide and ammonia on TiO_2 anatase. Appl Catal 64(1–2):243–257. https://doi.org/10.1016/S0166-9834(00)81564-X
93. Wu JCS, Cheng YT (2006) In situ FTIR study of photocatalytic NO reaction on photocatalysts under UV irradiation. J Catal 237(2):393–404. https://doi.org/10.1016/j.jcat.2005.11.023
94. Morales-Flórez V, Santos A, Romero-Hermida I, Esquivias L (2015) Hydration and carbonation reactions of calcium oxide by weathering: kinetics and changes in the nanostructure. Chem Eng J 265:194–200. https://doi.org/10.1016/j.cej.2014.12.062
95. Hüsken G, Hunger M, Brouwers HJH (2009) Experimental study of photocatalytic concrete products for air purification. Build Environ 44(12):2463–2474. https://doi.org/10.1016/j.buildenv.2009.04.010
96. Yu QL, Brouwers HJH (2009) Indoor air purification using heterogeneous photocatalytic oxidation. Part I: experimental study. Appl Catal B Environ 92(3–4):454–461. https://doi.org/10.1016/j.apcatb.2009.09.004
97. Kamran M, Sajjad M, Qadir S, Wang CL, Zhang RT, Ma BD, Bai ST (2025) Crystal facet engineering enhances photocatalytic NO_x abatement selectivity. Mater Sci Eng B Adv. https://doi.org/10.1016/j.mseb.2025.118206
98. Komazaki Y, Shimizu H, Tanaka S (1999) A new measurement method for nitrogen oxides in the air using an annular diffusion scrubber coated with titanium dioxide. Atmos Environ 33(27):4363–4371. https://doi.org/10.1016/S1352-2310(99)00231-9
99. Hadjiivanov K, Avreyska V, Klissurski D, Marinova T (2002) Surface species formed after NO adsorption and NO+O_2 coadsorption on ZrO_2 and sulfated ZrO_2: an FTIR spectroscopic study. Langmuir 18(5):1619–1625. https://doi.org/10.1021/la0110895
100. Ma H, Li DS, Li YY, Li YY, Wang CH, Zhang XT (2024) Atomically dispersed Mn sites on TiO_2(B) microspheres enables efficient photocatalytic abatement of NOx. Sep Purif Technol. https://doi.org/10.1016/j.seppur.2024.126357
101. Folli A, Bloh JZ, Armstrong K, Richards E, Murphy DM, Lu L, Kiely CJ, Morgan DJ, Smith RI, Mclaughlin AC, Macphee DE (2018) Improving the selectivity of photocatalytic NOx abatement through improved O_2 reduction pathways using $Ti_{0.909}W_{0.091}O_2N_x$ semiconductor nanoparticles: from characterization to photocatalytic performance. Acs Catal 8(8):6927–6938. https://doi.org/10.1021/acscatal.8b00521
102. Damma D, Boningari T, Ettireddy PR, Reddy BM, Smirniotis PG (2018) Direct decomposition of NO_x over TiO_2 supported transition metal oxides at low temperatures. Ind Eng Chem Res 57(49):16615–16621. https://doi.org/10.1021/acs.iecr.8b03532
103. Luévano-Hipólite E, Martínez-de la Cruz A (2016) Enhanced photocatalytic activity of TiO_2 rutile by coupling with fly ashes for the removal of NO gases. Ind Eng Chem Res 55(44):11512–11519. https://doi.org/10.1021/acs.iecr.6b03302
104. Al Mayyahi A, Sarker S, Everhart BM, He XQ, Amama PB (2022) One-step fluorine-free synthesis of delaminated, OH-terminated Ti_3C_2: high photocatalytic NO_x storage selectivity enabled by coupling TiO_2 and Ti_3C2-OH. Mater Today Commun. https://doi.org/10.1016/j.mtcomm.2022.103835
105. Fujiwara K, Pratsinis SE (2018) Single Pd atoms on TiO_2 dominate photocatalytic NO_x removal. Appl Catal B Environ 226:127–134. https://doi.org/10.1016/j.apcatb.2017.12.042
106. Kruczala K, Neubert S, Dhaka K, Mitoraj D, Jánosíková P, Adler C, Krivtsov I, Patzsch J, Bloh J, Biskupek J, Kaiser U, Hocking RK, Toroker MC, Beranek R (2023) Enhancing photocatalysis: understanding the mechanistic diversity in photocatalysts modified with single-atom catalytic sites. Adv Sci. https://doi.org/10.1002/advs.202303571
107. Ebrahimi E, Irfan M, Shabani F, Kocak Y, Karakurt B, Erdem E, Demir HV, Ozensoy E (2020) Core-crown quantum nanoplatelets with favorable type-ii heterojunctions boost charge separation and photocatalytic NO oxidation on TiO_2. ChemCatChem 12(24):6329–6343. https://doi.org/10.1002/cctc.202000749
108. Martins NCT, Angelo J, Girao AV, Trindade T, Andrade L, Mendes A (2016) N-doped carbon quantum dots/TiO_2 composite with improved photocatalytic activity. Appl Catal B Environ 193:67–74. https://doi.org/10.1016/j.apcatb.2016.04.016
109. Hensel J, Wang GM, Li Y, Zhang JZ (2010) Synergistic effect of CdSe quantum dot sensitization and nitrogen doping of TiO_2 nanostructures for photoelectrochemical solar hydrogen generation. Nano Lett 10(2):478–483. https://doi.org/10.1021/nl903217w
110. Bajorowicz B, Nadolna J, Lisowski W, Klimczuk T, Zaleska-Medynska A (2017) The effects of bifunctional linker and reflux time on the surface properties and photocatalytic activity of CdTe quantum dots decorated $KTaO_3$ composite photocatalysts. Appl Catal B Environ 203:452–464. https://doi.org/10.1016/j.apcatb.2016.10.027
111. Kelestemur Y, Olutas M, Delikanli S, Guzelturk B, Akgul MZ, Demir HV (2015) Type-II colloidal quantum wells: CdSe/CdTe core/crown heteronanoplatelets. J Phys Chem C 119(4):2177–2185. https://doi.org/10.1021/jp510466k
112. Zhao ZW, Sun YJ, Dong F (2015) Graphitic carbon nitride based nanocomposites: a review. Nanoscale 7(1):15–37. https://doi.org/10.1039/c4nr03008g
113. Barreca D, Gámiz B, Maccato C, Sánchez L (2025) Nanostructured systems to combat NO_x air pollution through Vis-light activated nanoarchitectonics: how, where and why…? Nanoscale. https://doi.org/10.1039/d5nr03181h
114. Dong F, Wang ZY, Li YH, Ho WK, Lee SC (2014) Immobilization of polymeric g-C_3N_4 on structured ceramic foam for efficient visible light photocatalytic air purification with real indoor illumination. Environ Sci Technol 48(17):10345–10353. https://doi.org/10.1021/es502290f
115. Wang XC, Maeda K, Thomas A, Takanabe K, Xin G, Carlsson JM, Domen K, Antonietti M (2009) A metal-free polymeric

photocatalyst for hydrogen production from water under visible light. Nat Mater 8(1):76–80. https://doi.org/10.1038/Nmat2317
116. Hu Z, Zhang YJ, Wang Y, Huang JS, Yang S, Li H (2024) Regulation of oriented NO photooxidation to circumvent NO2 with high-coordinated M-N5 (M = Fe Co, Mn, Ti) sites and far-carbon defects. Appl Catal B Environ Energy 5:346. https://doi.org/10.1016/j.apcatb.2024.123948
117. Irfan M, Sevim M, Koçak Y, Balci M, Metin Ö, Ozensoy E (2019) Enhanced photocatalytic NO_x oxidation and storage under visible-light irradiation by anchoring Fe_3O_4 nanoparticles on mesoporous graphitic carbon nitride (mpg-C_3N_4). Appl Catal B Environ 249:126–137. https://doi.org/10.1016/j.apcatb.2019.02.067
118. Wu XF, Cheng JS, Li XF, Li YH, Lv KL (2019) Enhanced visible photocatalytic oxidation of NO by repeated calcination of g-C3N4. Appl Surf Sci 465:1037–1046. https://doi.org/10.1016/j.apsusc.2018.09.165
119. Erdogan DA, Sevim M, Kisa E, Emiroglu DB, Karatok M, Vovk EI, Bjerring M, Akbey Ü, Metin Ö, Ozensoy E (2016) Photocatalytic activity of mesoporous graphitic carbon nitride (mpg-C_3N_4) towards organic chromophores under UV and VIS light illumination. Top Catal 59(15–16):1305–1318. https://doi.org/10.1007/s11244-016-0654-3
120. Groenewolt M, Antonietti M (2005) Synthesis of g-C_3N_4 nanoparticles in mesoporous silica host matrices. Adv Mater 17(14):1789. https://doi.org/10.1002/adma.200401756
121. Gu ZY, Jin MD, Wang X, Zhi RT, Hou ZH, Yang J, Hao HF, Zhang SY, Wang XL, Zhou EP, Yin S (2023) Recent advances in g-C_3N_4-based photocatalysts for NO_x removal. Catalysts. https://doi.org/10.3390/catal13010192
122. Yu MX, Chang SX, Ma L, Wu XF, Yan JT, Ding YB, Zhang X, Carabineiro SAC, Lv KL (2025) Remarkable improvement in photocatalytic activity of g-C_3N_4 for NO oxidation through surface hydroxylation. Sep Purif Technol. https://doi.org/10.1016/j.seppur.2024.128695
123. Duan YY, Wang Y, Gan LY, Meng JZ, Feng YJ, Wang KW, Zhou K, Wang C, Han XD, Zhou XY (2021) Amorphous carbon nitride with three coordinate nitrogen ($N3_C$) vacancies for exceptional NO_x abatement in visible light. Adv Energy Mater. https://doi.org/10.1002/aenm.202004001
124. Xia Y, Yang H, Ho WK, Zhu BC, Yu JG (2024) Promoting the photocatalytic NO oxidation activity of hierarchical porous g-C_3N_4 by introduction of nitrogen vacancies and charge channels. Appl Catal B Environ Energy. https://doi.org/10.1016/j.apcatb.2023.123604
125. Wang H, He WJ, Dong XA, Wang HQ, Dong F (2018) In situ FT-IR investigation on the reaction mechanism of visible light photocatalytic NO oxidation with defective g-C_3N_4. Sci Bull 63(2):117–125. https://doi.org/10.1016/j.scib.2017.12.013
126. Li KN, Zhou WC, Li XF, Li Q, Carabineiro SAC, Zhang SS, Fan JJ, Lv KL (2023) Synergistic effect of cyano defects and $CaCO_3$ in graphitic carbon nitride nanosheets for efficient visible-light-driven photocatalytic NO removal. J Hazard Mater. https://doi.org/10.1016/j.jhazmat.2022.130040
127. Ren YY, Li Y, Wu XY, Wang JL, Zhang GK (2021) S-scheme Sb_2WO_6/g-C_3N_4 photocatalysts with enhanced visible-light-induced photocatalytic NO oxidation performance. Chinese J Catal 42(1):69–77. https://doi.org/10.1016/S1872-2067(20)63631-2
128. Ahmadi K, Bathla A, Younis SA, Kim KH (2026) Engineered titanium dioxide-based photocatalysts for NO_x abatement: navigating design strategies and structure activity relationships for practical air purification. J Mater Chem A 14(2):852–879. https://doi.org/10.1039/d5ta06575e
129. Banerjee S, Pillai SC, Falaras P, O'Shea KE, Byrne JA, Dionysiou DD (2014) New insights into the mechanism of visible light photocatalysis. J Phys Chem Lett 5(15):2543–2554. https://doi.org/10.1021/jz501030x
130. Ji PF, Song Y, Drake T, Veroneau SS, Lin ZK, Pan XD, Lin WB (2018) Titanium(III)-Oxo clusters in a metal-organic framework support single-site Co(II)-hydride catalysts for arene hydrogenation. J Am Chem Soc 140(1):433–440. https://doi.org/10.1021/jacs.7b11241
131. Chen MJ, Wei XY, Zhao LL, Huang Y, Lee SC, Ho K, Chen KH (2020) Novel N/carbon quantum dot modified MIL-125(Ti) composite for enhanced visible-light photocatalytic removal of NO. Ind Eng Chem Res 59(14):6470–6478. https://doi.org/10.1021/acs.iecr.9b06816
132. Hu Z, Li XF, Zhang SS, Li Q, Fan JJ, Qu XL, Lv KL (2020) Fe_1/TiO_2 hollow microspheres: Fe and Ti dual active sites boosting the photocatalytic oxidation of NO. Small. https://doi.org/10.1002/smll.202004583
133. Yu JG, Wang SH, Low JX, Xiao W (2013) Enhanced photocatalytic performance of direct Z-scheme g-C_3N_4-TiO_2 photocatalysts for the decomposition of formaldehyde in air. Phys Chem Chem Phys 15(39):16883–16890. https://doi.org/10.1039/c3cp53131g
134. Balapure A, Dutta JR, Ganesan R (2024) Recent advances in semiconductor heterojunctions: a detailed review of the fundamentals of photocatalysis, charge transfer mechanism and materials. Rsc Appl Interfaces 1(1):43–69. https://doi.org/10.1039/d3lf00126a
135. Sudrajat H, Nobatova M (2024) Heterojunction photocatalysts: where are they headed? RSC Appl Interfaces 2:599–619. https://doi.org/10.1039/D5LF00037H
136. Salazar-Marín D, Oza G, Real JAD, Cervantes-Uribe A, Pérez-Vidal H, Kesarla MK, Torres JGT, Godavarthi S (2024) Distinguishing between type II and S-scheme heterojunction materials: a comprehensive review. Appl Surf Sci Adv. https://doi.org/10.1016/j.apsadv.2023.100536
137. Xu QL, Zhang LY, Yu JG, Wageh S, Al-Ghamdi AA, Jaroniec M (2018) Direct Z-scheme photocatalysts: principles, synthesis, and applications. Mater Today 21(10):1042–1063. https://doi.org/10.1016/j.mattod.2018.04.008
138. Sahoo SK, Acharya L, Biswal L, Priyadarshini P, Parida K (2024) Recent advancements in graphitic carbon nitride based direct Z- and S-scheme heterostructures for photocatalytic H_2O_2 production. Inorg Chem Front 11(16):4914–4973. https://doi.org/10.1039/d4qi00950a
139. Hu XS, Wang YW, Ling Z, Song HR, Cai Y, Li Z, Zu DY, Li CP (2021) Ternary g-C_3N_4/TiO_2/Ti_3C_2 MXene S-scheme heterojunction photocatalysts for NO_x removal under visible light. Appl Surf Sci. https://doi.org/10.1016/j.apsusc.2021.149817
140. Fareed I, Khan MD, Farooq MU, Akram M, Rehman SU, Anam HS, Zubair A, Li CB, Butt FK (2026) Photocatalytic NO_x abatement: a review of materials, mechanisms, and strategies. J Electron Mater 55(1):144–179. https://doi.org/10.1007/s11664-025-12455-9
141. Miranda C, Mansilla H, Yáñez J, Obregón S, Colón G (2013) Improved photocatalytic activity of g-C_3N_4/TiO_2 composites prepared by a simple impregnation method. J Photoch Photobio A 253:16–21. https://doi.org/10.1016/j.jphotochem.2012.12.014
142. Ma JZ, Wang CX, He H (2016) Enhanced photocatalytic oxidation of NO over g-C_3N_4-TiO_2 under UV and visible light. Appl Catal B Environ 184:28–34. https://doi.org/10.1016/j.apcatb.2015.11.013
143. Giannakopoulou T, Papailias I, Todorova N, Boukos N, Liu Y, Yu JG, Trapalis C (2017) Tailoring the energy band gap and edges' potentials of g-C3N4/TiO2 composite photocatalysts for NOx removal. Chem Eng J 310:571–580. https://doi.org/10.1016/j.cej.2015.12.102
144. Papailias I, Todorova N, Giannakopoulou T, Yu JG, Dimotikali D, Trapalis C (2017) Photocatalytic activity of modified g-C_3N_4/TiO_2 nanocomposites for NO_x removal. Catal Today 280:37–44. https://doi.org/10.1016/j.cattod.2016.06.032

145. Al Mayyahi A, Sekar A, Rajendran S, Sigdel S, Lu LY, Wang J, Wang GH, Li J, Amama PB (2023) Hierarchical TiO_2-g-C_3N_4 photocatalyst with purification effect for NO_x oxidation under cyan light. J Photoch Photobio A. https://doi.org/10.1016/j.jphotochem.2023.114965
146. Skalska K, Miller JS, Ledakowicz S (2010) Trends in NO_x abatement: a review. Sci Total Environ 408(19):3976–3989. https://doi.org/10.1016/j.scitotenv.2010.06.001
147. Mamaghani AH, Haghighat F, Lee CS (2017) Photocatalytic oxidation technology for indoor environment air purification: the state-of-the-art. Appl Catal B Environ 203:247–269. https://doi.org/10.1016/j.apcatb.2016.10.037
148. Ernam S, Akgül ZE, Üner D (2023) Recommendations for improving the experimental protocol for the determination of photocatalytic activity by nitric oxide oxidation measurements. Turk J Chem 47(5):1285. https://doi.org/10.55730/1300-0527.3612
149. Uner D, Bayar I, Tabari T (2015) The influence of relative humidity on photocatalytic oxidation of nitric oxide (NO) over TiO_2. Appl Surf Sci 354:260–266. https://doi.org/10.1016/j.apsusc.2015.07.045
150. International Organization for Standardization. ISO 22197-1-2016 fine ceramics (advanced ceramics, advanced technical ceramics)—test method for air-purification performance of semiconducting photocatalytic materials
151. Dudek D, Janus M (2022) Photoactive cements: a review. Materials. https://doi.org/10.3390/ma15155407
152. Liu HX, Mei H, Miao NX, Pan LK, Jin ZP, Zhu GQ, Gao JZ, Wang JJ, Cheng LF (2021) Synergistic photocatalytic NO removal of oxygen vacancies and metallic bismuth on $Bi_{12}TiO_{20}$ nanofibers under visible light irradiation. Chem Eng J. https://doi.org/10.1016/j.cej.2021.128748
153. Braslavsky SE (2007) Glossary of terms used in photochemistry 3rd edition (IUPAC recommendations 2006). Pure Appl Chem 79(3):293–465. https://doi.org/10.1351/pac200779030293
154. Kisch H, Bahnemann D (2015) Best practice in photocatalysis: comparing rates or apparent quantum yields? J Phys Chem Lett 6(10):1907–1910. https://doi.org/10.1021/acs.jpclett.5b00521
155. Chen XB, Shen SH, Guo LJ, Mao SS (2010) Semiconductor-based photocatalytic hydrogen generation. Chem Rev 110(11):6503–6570. https://doi.org/10.1021/cr1001645
156. Henderson MA (2011) A surface science perspective on TiO_2 photocatalysis. Surf Sci Rep 66(6–7):185–297. https://doi.org/10.1016/j.surfrep.2011.01.001
157. Ren YJ, Harold MP (2011) NOx storage and reduction with H2 on Pt/Rh/BaO/CeO2: effects of Rh and CeO2 in the absence and presence of CO2 and H2O. Acs Catal 1(8):969–988. https://doi.org/10.1021/cs200252r